UNIVERSITY OF OKLAHOMA

GRADUATE COLLEGE

HIGH RESOLUTION MICROSCOPY OF ANTIMONIDE HETEROSTRUCTURES AND STREPSIPTERA EYES

A THESIS

SUBMITTED TO THE GRADUATE FACULTY

in partial fulfillment of the requirements for the Degree of

MASTER OF SCIENCE

By

DAMIEN RICHERT
Norman, Oklahoma
2019

HIGH RESOLUTION MICROSCOPY OF ANTIMONIDE HETEROSTRUCTURES AND STREPSIPTERA EYES

A THESIS APPROVED FOR THE
DEPARTMENT OF ENGINEERING PHYSICS

By

Dr. Michael Santos

Dr. Preston Larson

Dr. Braden Abbott

Acknowledgments

Firstly, I would like to thank my advisor Dr. Michael Santos for all his knowledge, advice and support which play a decisive part in the completion of this work. I appreciate the great work environment he provides me.

I am thankful to Dr. Preston Larson for his large contribution at every stage of this project as well as the advice he gave me on the following work.

My kind regards to Dr. Braden Abbott for being part of my committee.

A special thanks for Tetsuya Mishima and Marisano James for providing the different structure and helping me understand the motivations behind the study of them.

I want to thank Joyce Hulin and all the faculty and staff of the department of Physics and Astronomy for their help during my stay at the University of Oklahoma.

I am also thankful to Dr. Jean-Pierre Fontaine for helping me before and throughout my stay here. I would like to thank Dr. Yamina Andre, Dr. Bernard Gruzza and Dr. Jol Leymarie to agreeing to be my French committee.

I want to thank my family for their love as well as financial and emotional support in spite of the distance.

Contents

List of Figures

List of Tables

List of Equations

Abstract

This thesis is structured into two independent parts, both using microscopy techniques. The first part uses SEM and AFM to characterize some electronic devices while the other deals with the study of the vision system of Strepsiptera bugs.

Part I: Microelectronic devices

The observation of solid state electronic devices by surface microscopy technique is critical for their characterization. Indeed, in-situ observation during the growth and subsequent X-ray diffraction does not provide all the relevant information about the crystalline structure and the state of the surface. One of the important topics in semiconductor science these last years has been quantum structures. It is especially used to develop better optoelectronic solid state devices such as lasers. As the technology progresses, new devices become more and more complicated to grow. The first chapter will focus on the characterization of the surface state of the grown samples. The samples are calibration structures for infrared detectors and infrared lasers. The observation of the surface is important as it gives us complementary information about crystalline quality as well as the size and concentration of defects. For optoelectronic devices, defects are often primary spots for recombination and can, therefore, drive the device yield down. As the layers studied are part of the buffer region rather than the active region, we do not have this issue. Nevertheless, defects in this region will cause others to appear in the subsequent layers grown on top of them. For this reason, knowing the state of the sample's surface at this stage in the growth is critical. We used field emission Scanning Electron Microscopy (FE-SEM) and Atomic Force Microscopy (AFM) to characterize the surface. These two technologies complement one another for our application. SEM gave us information about the crystalline configuration of the defects on the sample surface while the AFM is great to provide precise information on the size of the defects.

The acquired data show a trend in in the density of surface features as a function of the mismatch coeffi-

cient and the ratio of actual thickness to critical thickness of the epilayer. The density of surface features decreases with those two parameters. And when the thickness of the epilayer is smaller than its critical thickness, we do not observe any surface features similar to a defect.

Part II: Biological sample

The second part of this thesis deals with biological material. We work in collaboration with Marisano James, a Ph.D. student, on the eye structure of Strepsiptera. The main goal was to collect three-dimensional data about the structure which is helpful to determine whether the eye has a compound structure. To achieve this objective, we used the Focused Ion Beam integrated with the Zeiss Neon SEM to etch away layers of the surface while taking images at each point in the process. By doing numerical treatment to these images, we can extract the shape of the retina and learn more about the eye structure. Unfortunately, the z resolution of our data set was not high enough and therefore, we cannot determine the structure. Nevertheless, we did learn about the distribution of the pigment in the eye.

Part I

Diverse Microelectronic Devices

Chapter 1

Surface defects on GaAsSb epilayers on GaAs substrate

1.1 Introduction

The microelectronics revolution has considerably changed our way of life. The progress made in this field has allowed us to live in a world with the easiest access to information ever. As this technology matures, there are more and more possible semiconductor structures we can make. It is particularly true in the optoelectronics field. For example, lasers are becoming more and more efficient, smaller and can operate in a wider wavelength range. This is partly due to the fact that quantum structures are realizable. They rely on the possibility of stacking layers with different lattice constants which eventually creates some crystalline defects. The goal of this thesis is to determine whether the degree of lattice mismatch between the epilayer and substrate can be detected on the sample surface using standard microscopy techniques. We studied GaAsSb on GaAs calibration structures grown by Molecular Beam Epitaxy because this set of samples have a large range in their mismatch coefficients. Those calibration samples will be used for optimizing the MBE growth parameters for future superlattice laser structures. We used the Atomic Force Microscope to study the roughness of the surface and the shapes of the defects.

Scanning Electron Microscopy was also been used to study the defects and gave us information about the Burger's vector and the minimal energy required for relaxation defects to appear. We also used Backscattered Electron Diffraction patterns to get information about the crystalline orientation of the sample and its surface defects.

1.2 Background

To understand the content of this part we need to define some notions first. The samples are calibration structures for a project on infrared lasers and detectors. We need to understand the techniques used to grow them and why the calibration was required. We also want to know what parameters are the most critical for an optoelectronic device such as a cascade laser.

1.2.1 Molecular Beam Epitaxy

The semiconductor material growth process is called epitaxy. There are several categories of epitaxy which differs by their growth rate, the smoothness of the obtained material and other parameters. Molecular Beam Epitaxy (MBE) has the lowest growth rate which allows precise control of the sample morphology [1]. This technique is used when the degree of lattice mismatch between two layers is important or when we have a low tolerance for the different layer thickness. The low substrate temperature as well as the slow growth rate, typically less than one monolayer per second reduces the probability of defects formation. Now that we explained the advantages of this technique let's focus on how it works. As shown in figure 1.1, an MBE growth chamber is composed of a wafer holder, multiple effusion cells, an electron gun, and a vacuum system. The principle of this technique is to put the wafer in a very high vacuum environment and to project directional atom beams on it. The vacuum is obtained by a combination of pumps. First, we establish a rough vacuum with a mechanical pump, then a high vacuum thanks to a turbo-molecular pump and finally a very high vacuum is created with a cryo-pumps and a sputter

ion pump. The level of vacuum is measured by an ion gauge [1]. The typical value of vacuum used is $1.33 * 10^3$ Pa. The high vacuum is required to have the longest mean free path for the material beams. It is also a condition to maintain the high purity level of the device structure.

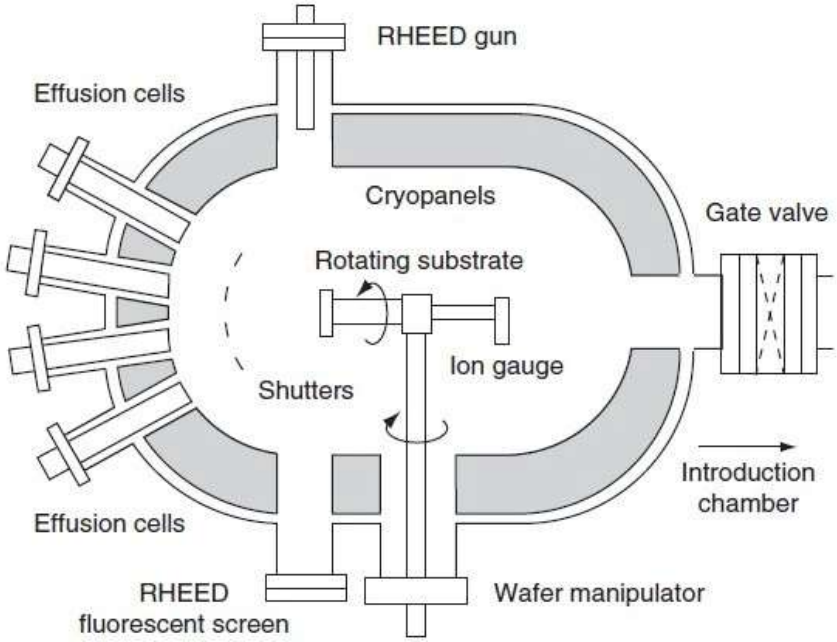

Figure 1.1: Diagram of Molecular Beam Epitaxy growth chamber, [1]

We use MBE technology because we want a degree of high control on the composition of each layer which is possible only if the material is grown in an ultra-high vacuum environment. The molecular beam is obtained by heating the effusion cell to a temperature where the contained material is slowly evaporated. As the growth rate is directly linked to the flux of this beam, we want the flux as steady as possible. The effusion cell heating is monitored by a thermocouple and a closed-loop control system is implemented to help stabilize the flux. When it has reached the desired condition, we open the shutter placed in front of the effusion cell which allows the beam to impinge on the substrate wafer.The atoms will find preferred sites on the surface of the wafer and this is how the structure grows. As it is an on-off system at a very slow growth rate, it allows us to have precise control over the composition of the structure.

Let's say we want to grow a GaAsSb layer on an InAs layer of 20nm. We would set up the growth rate lower than one atomic monolayer per second controlled by a series of calibration structures and switch from the InAs effusion cell to the GaAsSb one after the time required to grow the 20nm layer. It is a well-controled process for a simple III-V alloy (One element of the third column of the periodic table of the element with of the fifth) because element V has to be in presence of the element from the third column to deposited. So, the growth is defined by the flux of element III. But in our case where we have an alloy with two elements from the fifth column, these elements V will compete to be deposited. So not only, we have to control precisely the flux of element III but we also have to control the flux of element V to have the desired composition. There are so many parameters with each its own degree of uncertainty that computation can not give us directly the correct setup. So, a calibration step is required in order to obtain those parameters. Because some change in the growth condition may occur with time (Chamber opened, power shortage, level of material in the effusion cells), the calibration step has to be done on a regular basis. A calibration is a way to fix an observed shift in the composition of the grown structure III-V. For reference, the MBE used by Dr. Santos group is a model from Veeco Instrument Inc.

1.2.2 Photoelectronic devices

A photoelectronic device is used when we need to switch between electrical and light signals. Some noteworthy examples of this technology are lasers, photodetectors, and photovoltaic cells. These devices are made of semiconductor material. To understand how photoelectronic devices work, we need to define the term semiconductor. We can classify solids into three categories: insulators, semiconductors, and conductors. The figure 1.2 shows the difference in the band structure of these materials.

A band is a range of energy state where charge carriers are allowed to be and are determined by statistical physics. A semimetal is a conductor because its valence and conduction band overlap allowing electrons to pass from one atom to another without any band requirements. In an insulator or semiconductor material, these bands are separated by a band gap. The difference between a semiconductor and an

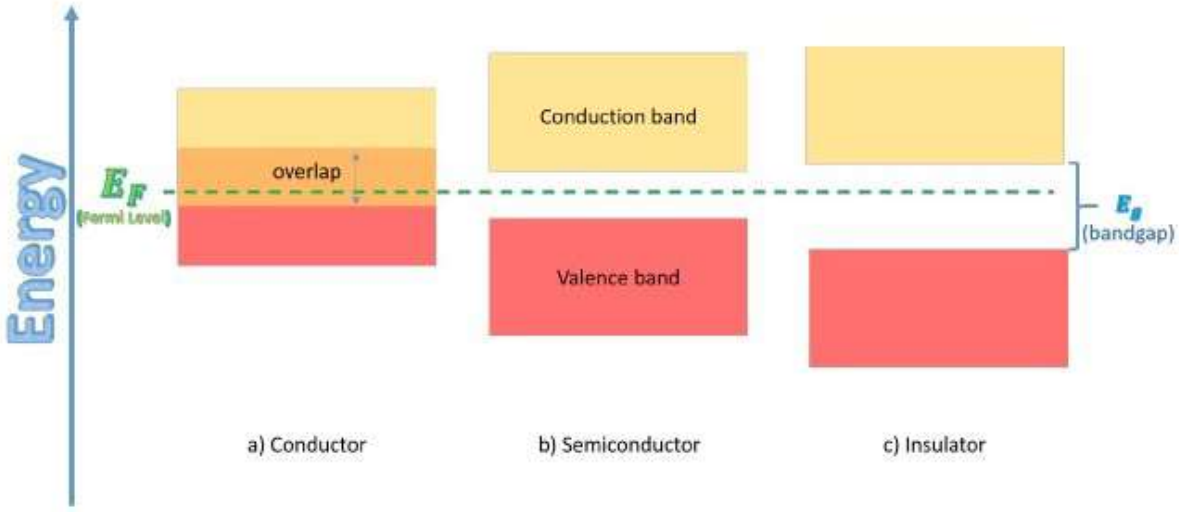

Figure 1.2: Solid material sorted by band structure, [2]

insulator is the width of the band gap. For an insulator, the bandgap is large enough to prevent thermal excitation of electrons from valence to conduction bands. But for semiconductors, it is narrow enough for significant thermal excitation at room temperature as well as excitation through absorption of infrared or visible light. A photoelectronic device uses this latter property. In this part, we are focusing on a structure of $GaAs_xSb_{1-x}$ grown on an InAs substrate and $InAs_{1-x}Sb_x$ grown on a GaSb substrate. This kind of material is used as a light emitter or detector at a specific wavelength in the infrared range [18].

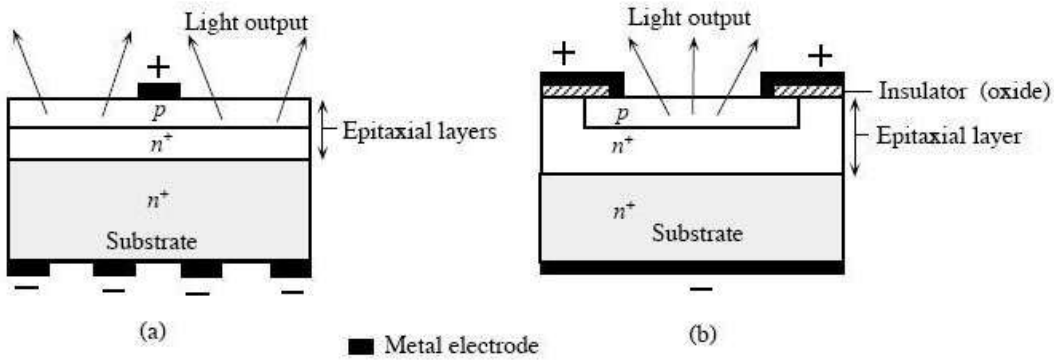

Figure 1.3: Principle of a LED, (a): a p layer is grown on top of a heavily doped n-substrate, (b): after processing, the device is obtained [3]

To do so, we create a PN diode as shown in figure 1.3. Electrified contact is made on the P and N layers and by applied an electric potential which leads to the formation of an electron-hole pair. Eventually, the carriers will return to a lower energy state and this phenomenon is responsible for the light emission. Indeed, to satisfy the energy conservation law, the carrier can either emit a phonon either a photon. This report will only deal with photon emission. In basic devices, i.e non-laser LED, the photon emission is due to the recombination of electrons and holes. For this to happen, electrons and holes have to be in the same physical region. Because of the way the device is engineered, there is a very low amount of minority carriers in each of the regions and so the odds of recombination are low. To increase this probability, we put a current between the two layers so electrons will be injected into the P doped region. The electrons have a higher mobility than the holes, so it is easier to have recombination events by making a few electrons passing through a high density of holes than by having the holes try to reach out for the electrons. The wavelength emitted is defined by the Planck-Einstein relation (1.1)

$$\lambda = \frac{hc}{E_g} \tag{1.1}$$

Where λ is the wavelength, h the plank constant, c the speed of light in the vacuum and E_g is the energy gap between valence and conduction band.

1.3 sample description and expectation

The samples we studied are calibration structures for detector and laser devices. The purpose of these structures was to find the ideal growth temperature and the ratio of As flux to Sb into the growth. Indeed, we can compute the $GaAs_xSb_{1-x}$ to achieve a lattice match with the InAs substrate, but we need to go through a calibration step to determined the flux needed to obtain the desired composition. As the lattice constant of the alloy depends on its composition, each calibration sample is measured by X-Ray diffraction after growth, which gives us a rocking curve as shown figure 1.4. These measurements give

us information on the lattice constant of the sample. We can see the intensity of the diffracted X-ray is maximized for a few values of the angle of incidence θ.

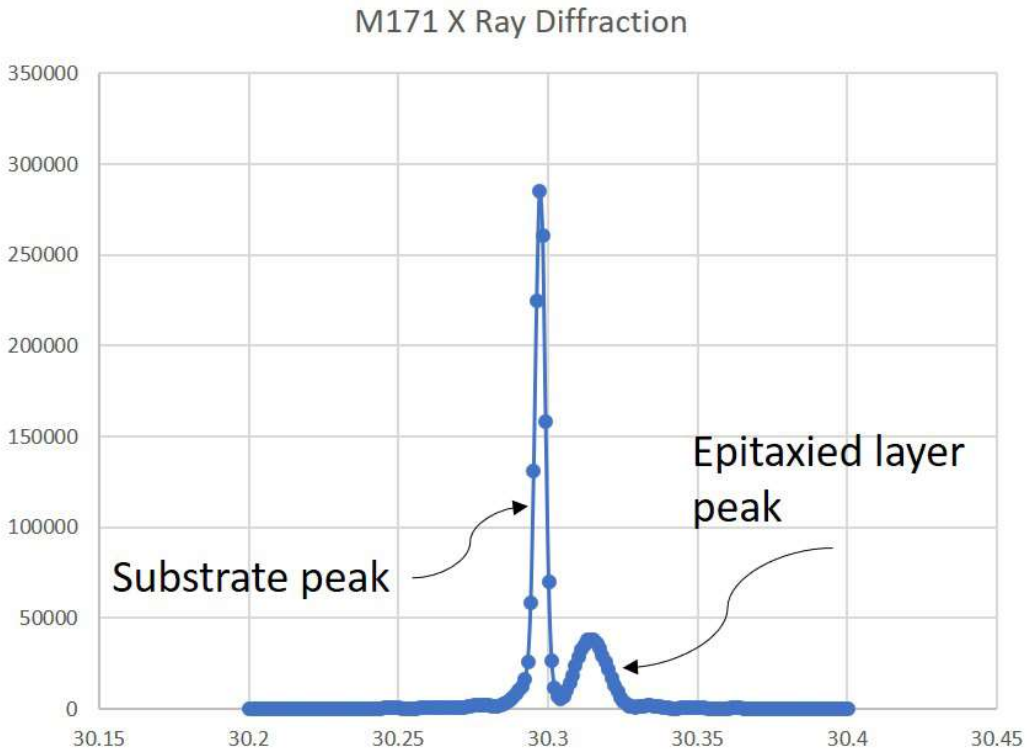

Figure 1.4: X-Ray Diffraction of M171 sample with diffraction peak from the substrate and from the epilayer

X-ray diffraction obeys Bragg's law which states there are diffraction maxima when the equation 1.2 is satisfied.

$$2dsin(\theta) = n\lambda \tag{1.2}$$

Here, d is the interplanar distance, λ the wavelength of the X-ray and n an integer called diffraction index. We know n, λ and θ so we can compute d. Knowing the crystalline structure of GaAs and GaSb is Zincblende, we can determine its lattice constant and therefore its composition. Because Zincblende is a cubic structure, we can state that d is defined by equation 1.3 where h, k and l are the Miller indices

of the Bragg plane and a is the lattice constant of the alloy.

$$d = \frac{a}{\sqrt{h^2 + k^2 + l^2}} \tag{1.3}$$

By combining the equation 1.2 and 1.3, we can get the lattice constant of the alloy. As we know that the lattice constants of GaAs and GaSb are 5.6532$\mathring{A}$ and 6.0959$\mathring{A}$ respectively [19] and because the difference between the two is not too large, we can use linear interpolation to find the composition of the $GaAs_xSb_{1-x}$ layer for the obtained lattice constant. In subsequent growth, we adjust the growth condition to have a more well-defined peak and shift composition to position the peak closer to where the simulated curve tells us it should be. The highest intensity peak is usually generated by the substrate layer which is the thickest and therefore returns the largest signal. The second peak we can see in Figure 1.4 is due to the epilayer. As the objective here is to find the growth parameter allowing to have a lattice match epilayer, we want those two peaks to occur at the same angular position. We can notice that the epilayer peak is at the right of the substrate one. It means that the lattice constant of the epilayer is larger than the substrate's lattice constant and so is tensile strained. If it were on the left side, the epilayer would be compressively strained. In our case of an MBE grown structures, the substrate temperature plays a role in the growth quality [1] and therefore in the defect concentration. It is a trial and error process. One of our goals for this study is to determine whether we can use standard microscopy techniques to see a difference on the surface features of the sample as a function of it lattice mismatch coefficient. Due to the trial and error nature of the process, some samples are far from the target. The largest ratio epilayer thickness to critical thickness has been observed on a $GaAs_xSb_{1-x}$ grown on InAs substrate sample (M126) where it was 43.1. At the opposite side of the range, we find M129 where the epilayer is only 2.8 times thicker than the critical thickness. For the second structure, as the thickness of the epilayer actually changes between the sample, this information is not pertinent.

1.3.1 Structures information

Two different structures have been grown on substrates of crystalline orientation (0 0 1). They are presented in the Figure 1.5.

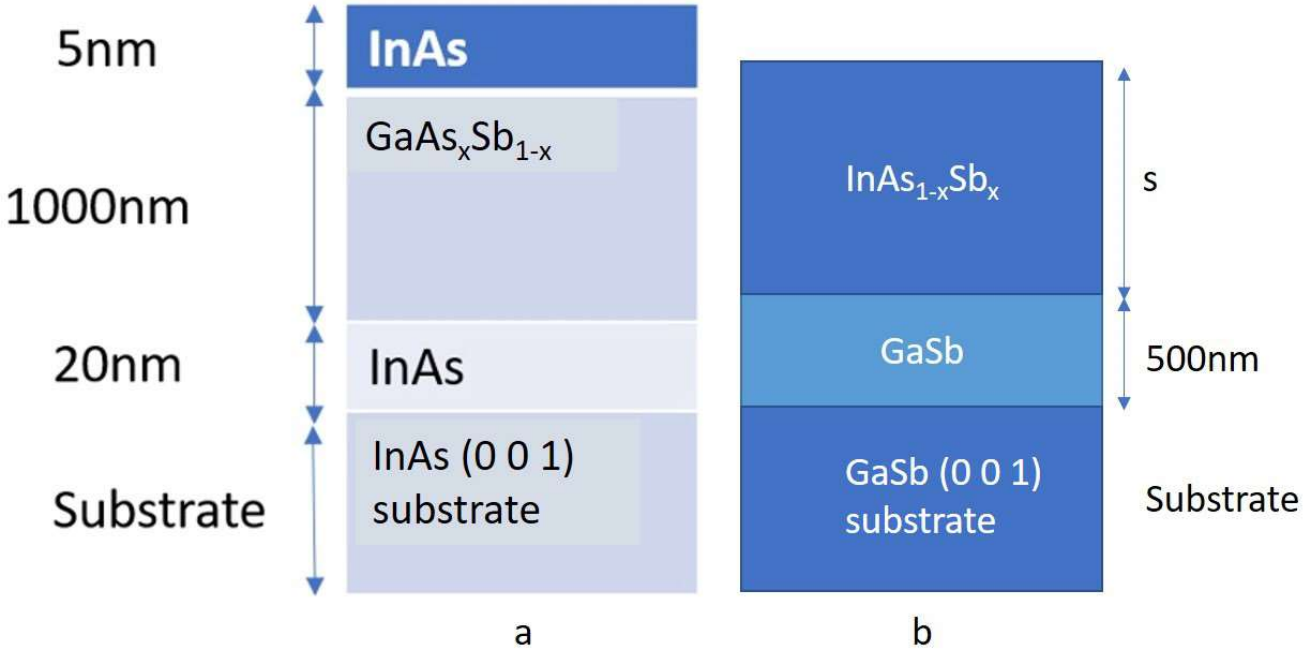

Figure 1.5: Layer structure of the studied devices

The first set of structures studied are composed of a layer of $GaAs_xSb_{1-x}$ grown by MBE on an InAs wafer. The difference between the samples is on the proportion of GaAs and GaSb. This layer's lattice parameter is a function of this proportion and is given by the equation 1.4.

$$a_{GaAs_xSb_{1-x}} = x * a_{GaAs} + (1-x) * a_{GaSb} \tag{1.4}$$

The second set of samples are composed of a layer of $InAs_{1-x}Sb_x$ grown by MBE on a GaSb wafer. For this set, both the thickness of the epilayer and its composition change We want the lattice constant of this layer to be as close as possible to the lattice constant of the substrate material. The table 1.1 shows the composition and alloy layer thickness of each of the grown structure. For each of them, we computed

the actual lattice constant of the alloy as well as its mismatch coefficient in relation to the lattice constant of the wafer. We also compute the composition of the alloy for the case it has the same lattice mismatch than the wafer.

sample name	M126	M123	M127	M122	M129	optimal
x	0.154	0.024	0.145	0.031	0.078	0.0849
lattice constant (Å)	6.027	6.085	6.031	6.082	6.061	6.058
Mismatch coefficient	5.04	4.45	4.39	3.94	0.51	0

(a)

sample name	M171	M189	Optimal
x	0.0831	0.015	0.0893
Thickness of the layer	300nm	1200nm	
lattice constant (Å)	6.027	6.085	6.0959
Mismatch coefficient	0.42	0.15	0

(b)

Table 1.1: (a): composition and lattice mismatch for $GaAs_xSb_{1-x}$ over InAs; (b): composition and lattice mismatch for $InAs_{1-x}Sb_x$ over GaSb

1.3.2 Surface state

We would like to have the smoothest surface possible because the more defects we get, the less efficient is the infrared device. The theory gives us the band-gap energy as a function of the composition of the material. In the real world, a high density of impurities can change this value, but this is not the case with our samples. Nevertheless, we still have some defects from strain relaxation. When we grow a layer with a different lattice constant than the wafer used as the substrate, the epilayer will adapt its lattice constant

to the wafer one. This phenomenon can be shown in figure 1.6.

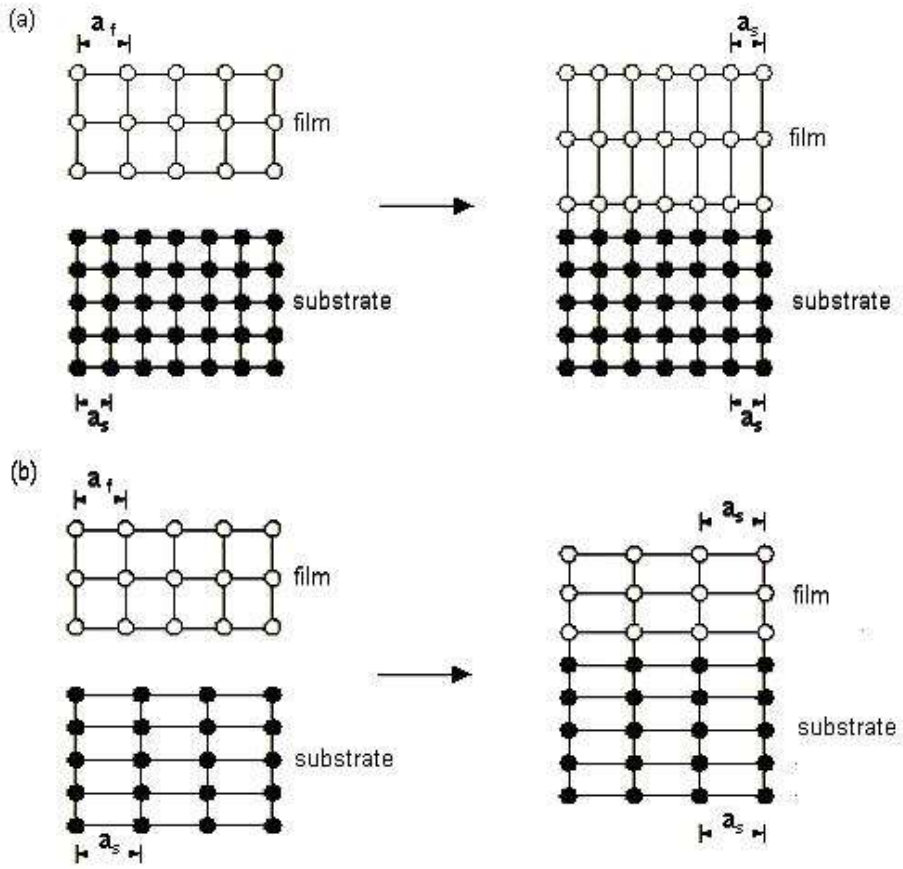

Figure 1.6: pseudomorphic growth of a film on a substrate. The film can be (a) compressively or (b) tensile strained in the growth plane, [4]

By adapting its lattice constant, the epilayer will store some energy in its lattice. This energy will continue to build up as we grow more and more of the layer [20]. As long as this energy is below the interfacial energy, no relaxation effect should appear in the structure. We can see the figure 1.6 shows two configurations. One is compressive in-plane which means that the lattice parameter of the top layer is larger than the wafers one and so the top layer is compressed in the x-y plan. When the lattice parameter of the film is smaller than the one of the wafer, we call it tensile in-plane because the top layer is made wider. In both case, the more the epilayer lattice constant differs from the substrate one, the more deformation energy will be generated. In other words, to avoid the formation of strain relaxation

defects, we want the epilayer to be perfectly lattice match with the substrate. It is important because defects are privileged recombination spots that worsen infrared device performance. Another parameter we have to deal with is the fact that the lattice parameter can also slightly change the band gap energy of the material [4]. We made a quick measurement of the density of these relaxation defects by an optical microscope. This measurement has been done with a technique called Differential Interference Contrast (DIC) or Nomarski microscopy.

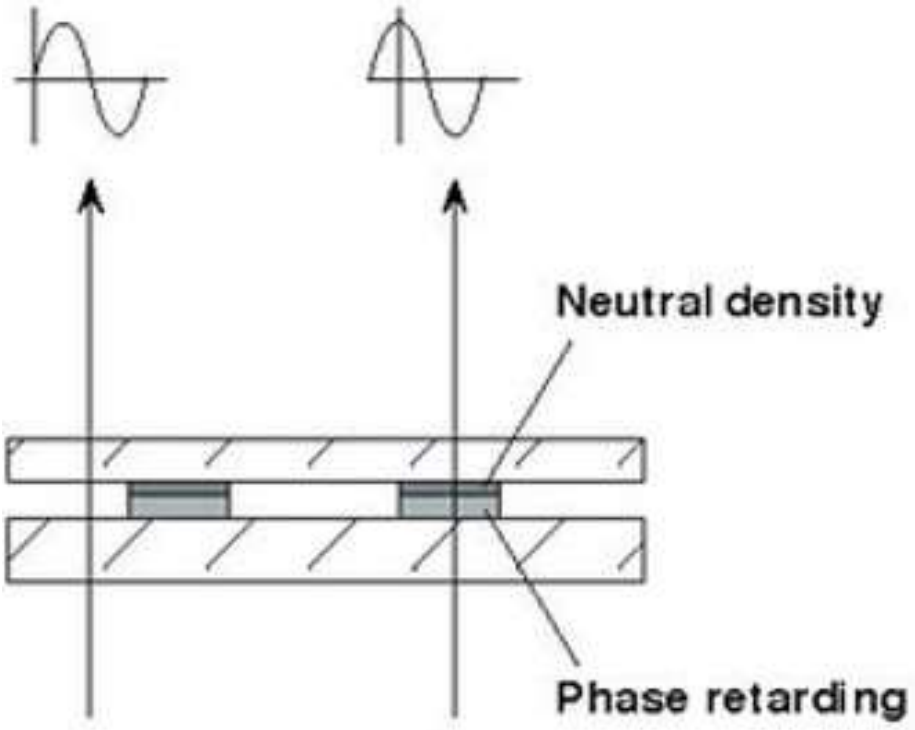

Figure 1.7: Principle of the DIC Microscope, [5]

As its name indicates, it uses interference to image the sample. Figure 1.7 shows the principle of this technique. The photon beam is divided into two beams, one for reference and the other passing through the sample. As the sample has a higher diffraction index than the air, the photon velocity will be slower while passing through it, creating a change in the phase compared to the reference beam. The difference between the two phases ($\Delta\phi$) remains constant when the beam exits the sample. So this difference is

a function of the thickness of the sample where the beam passed. In the end, the reference beam and sample beam are combined into a diffraction pattern. We know that a dark spot will appear where $\Delta\phi = (2n+1)\pi$ and a bright spot will appear where this difference is equal to 2nπ. Figure 1.8 shows the surface feature of one of the structures (M123) as seen in DIC images. Each spot is a single defect.

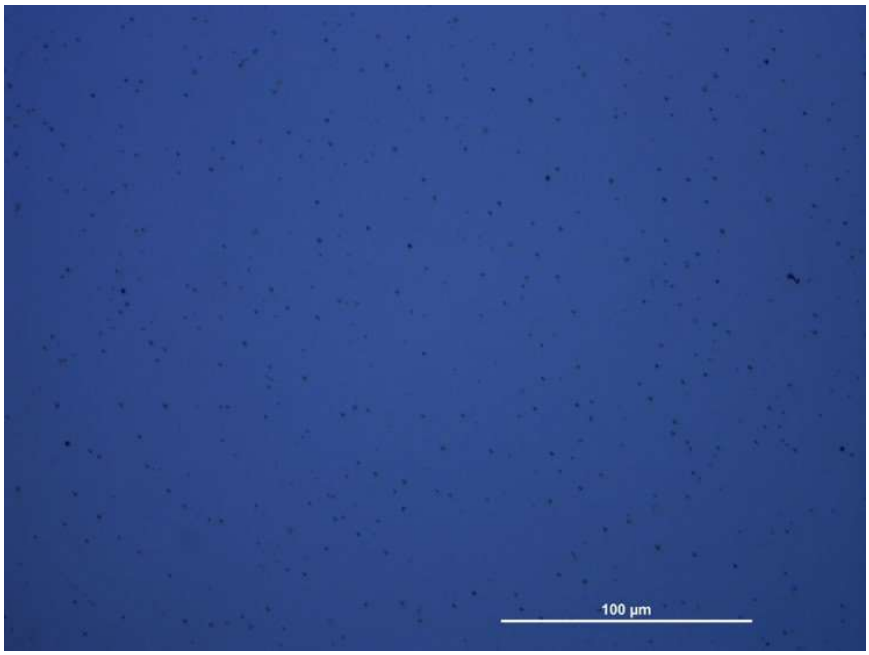

Figure 1.8: Surface view of sample M123 obtained by DIC

We then obtain the defect density by counting how many of them are in a given area. We can see from figure 1.9 that the lower is the mismatch, the lower the defect density is. The negative lattice mismatch coefficients refer to tensile in-plane structures while the positive ones are corresponding to the compressive in-plane structures. The minimal defect density is for M129 with a lattice mismatch of 0.00051. We can see in this first part that the defect density decreases with the lattice mismatch. This is an expected result although these defect densities are high for MBE grown material.

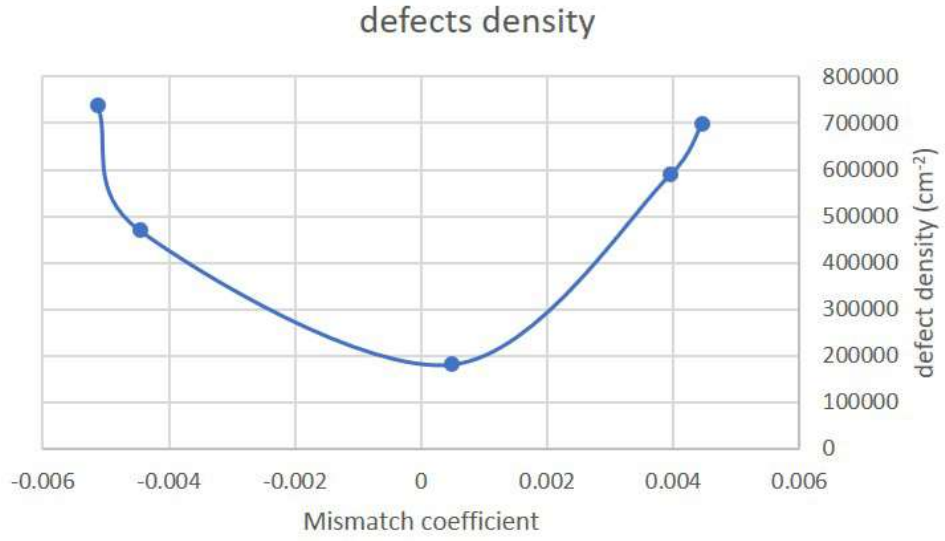

Figure 1.9: Defect density as a function of the mismatch (positive sign in the horizontal axis is for compressive in-plane structures while negative sign is for tensile in-plane structures)

1.3.3 Defect categories

There are different regimes to defect formation. If the lattice parameter of the grown material differs too much from the wafer one, the relaxation will occur by Cross-hatch defect formations. As the ratio thickness over critical thickness increase, the epilayer lattice parameter become closer and closer to its original value. It will eventually reach the point where it is fully relaxed. When it is the case, we don't see any crosshatch at the surface and the amount of defect should go down as the thickness of this layer keeps increasing. People use this fact when they grow a buffer layer.

1.4 Scanning Electron Microscopy

We used scanning electron microscopy (SEM) to get information about the shape of the defects and their crystalline orientation. This work has been done with the Zeiss Neon EsB SEM. SEM uses an electron beam to scan the surface of the sample by counting the number of particles resulting from the interactions between the electron beam and the one from the bulk of the sample. Usually, the size of the

beam in the x-y direction is 1nm. It can change depending on the conditions of the measurement [21].

1.4.1 Background

When we put a sample in a SEM, there are several parameters we can play with to get the best image. In order to choose them wisely, we need to define what we want to observe. We are interested in the shape of the defect. This information is mostly topographical as the defect is defined by a z variation. The SEM has different imaging modes. The interaction between the incident electron beam and the sample will generate different type of particles, each of them can be used to get information. As the type of information we get depends on the particles read, we refer the imaging mode by the particles it will used.

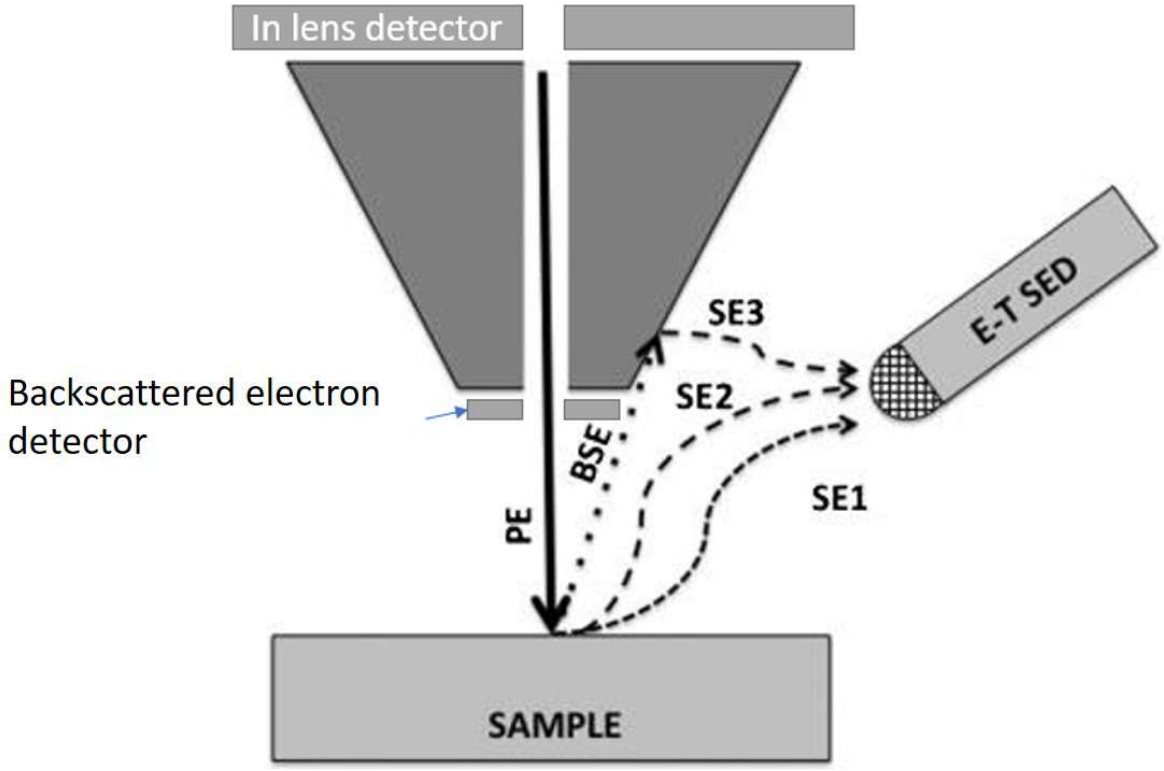

Figure 1.10: SEM imaging mode, form [6]

One can see in figure 1.10 that there is two type of electrons resulting from this beam-sample interaction.

In addition to the backscattered electron (BSE) and the secondary electron (SE), X-Ray photons and Auger electrons will also be generated. Those two later particles give us information about the composition of the sample. As we already got this data by X-Ray diffraction, we will not explain their formation either their detection. We only used BSE and SE images. Backscattered electron imaging gives us compositional and crystalline information on the sample. Backscattered electrons are due to near elastic collisions between the electrons of the incident beam and the atoms of the sample. The higher the atomic number of the atom is, the higher is the probability to have an elastic collision. Therefore we have a mechanism for compositional contrast. Crystalline information can be obtained by an interaction between the incident beam and the crystal structure known as Electron Channeling [22]. This technique will be explained and used later. The other mode is using the secondary electron signal. Secondary electrons are created in the beam-specimen interaction volume. When an electron strikes the sample surface, it will ionize some of the atoms. Depending on the energy of the incoming electron, it can interact with atoms at a given depth from its impact point.

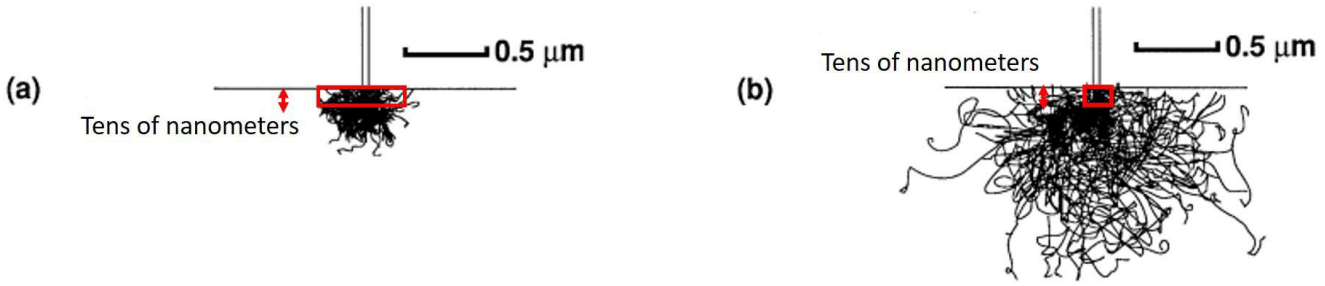

Figure 1.11: Monte Carlo simulation of the trajectory of the incident electrons in the interaction volume in function of the accelerating voltage. (a) 10keV, (b) 20keV. Only the electron generated into the red rectangle ($\sim$ 50nm deep) can make their way outside of the bulk, [7]

As the energy of the incoming beam depends on the acceleration voltage, the interaction volume can be reduced by changing the acceleration voltage as one can see on figure 1.11. When we make the interaction volume smaller, the electrons are generated in a smaller volume and therefore the z-resolution

increases [7]. The topographical information comes from the fact that the secondary electrons generated below the surface of the sample have to make their way through the material to reach the surface where they can easily get to the detector. So only the electrons generated close to the surface can escape from the sample bulk and be detected. Because of the number of pamameter that this volume thickness depends on, we cannot have an exact value but it is of the order of tens of nanometers [21]. As the volume close to the surface of the sample is a function of the topography of the sample, the secondary electron signal gives us information on that aspect. We can notice in figure 1.11 that the top of the interaction volume gets slightly larger when the acceleration voltage decrease. Therefore, the x, y resolution decrease slightly with the acceleration voltage. In the first part of our study, we focused on the topographic information so we used a secondary electron detector. We next need to choose the proper detector between the two. We used an in-lens secondary detector which gives us the highest secondary over backscattering electron ratio [6]. Once we define which imaging mode to use, we need to choose an appropriate acceleration voltage. Thanks to Abbe's equation (1.5, [21]), this parameter affects the resolution limit.

$$d = \frac{0.612\lambda}{n * sin(\alpha)} \tag{1.5a}$$

$$\lambda = \frac{1.23}{\sqrt{V}} \tag{1.5b}$$

$$d = \frac{0.752}{n * sin(\alpha) * \sqrt{V}} \tag{1.5c}$$

Here, d is the diffraction limited resolution in nm, λ is the electrons wavelength in nm, α is the half aperture angle V is the acceleration voltage in eV and n is the index of refraction of the medium. For SEM, the electron beam is in a high vacuum environment so n=1. The second is obtained by a combination of De Broglies equation and the classical kinetic energy equation [21]. Indeed, for the acceleration voltage usually applied in SEM, we can neglect the relativistic effect. We can see from this equation that if we increase the accelerating voltage, we reduce d and so increase the maximum resolution reachable. Typically this optimal resolution is in the range of one to tens of nanometers. But we just saw that a higher acceleration voltage will decrease the depth resolution of the picture. So, we must compromise.

Table 1.2 shows the influence that the acceleration voltage has on different parameters.

Acceleration Voltage	depth resolution	diffracted limited spacial resolution
Low	High	Low
High	Low	High

Table 1.2: influence of the acceleration voltage on the resolution, the signal over noise ratio and the diffraction limited resolution

One typical value for V in this kind of measurement where we want a few nanometer probe size and a very surface sensitive measurement is 10kV. We also need to optimize the signal to noise ratio. This could be done by choosing a slower scanning rate (scan speed 7 or 8, ˜ 0.16 ms spent on each point) and select line integral noise reduction on the image acquisition software. These parameters are good for direct imaging but in the second part where we aim for a diffraction pattern, we will increase the emission current and use a larger aperture. Indeed, in the case of a diffraction image, the signal to noise ratio can be more critical than the spatial resolution.

1.4.2 Shape of the defects

Once we define all the parameters, we can start imaging. We made sure the edge of the sample were parallel to edge of the scanned area. We can see on figure 1.12 that the defect edges are slanted of an angle $\pi/4$ in respect to the edge of the picture. We know that the samples have been cleaved along the crystalline plane (1 0 0). So, if the defect edge forms a $\pi/4$ angle with the edge, its crystalline orientation has to be [1 1 x]. At this point in the study, we do not have enough information to conclude about the z component of the orientation of the facet of the defect. Later electron backscattered diffraction pattern will give us the full information about the crystalline orientation of those defects. We collected images from all the sample but couldn't spot any difference in the defect shape. We can also say that the defect is on the top of what looks like dislocation lines.

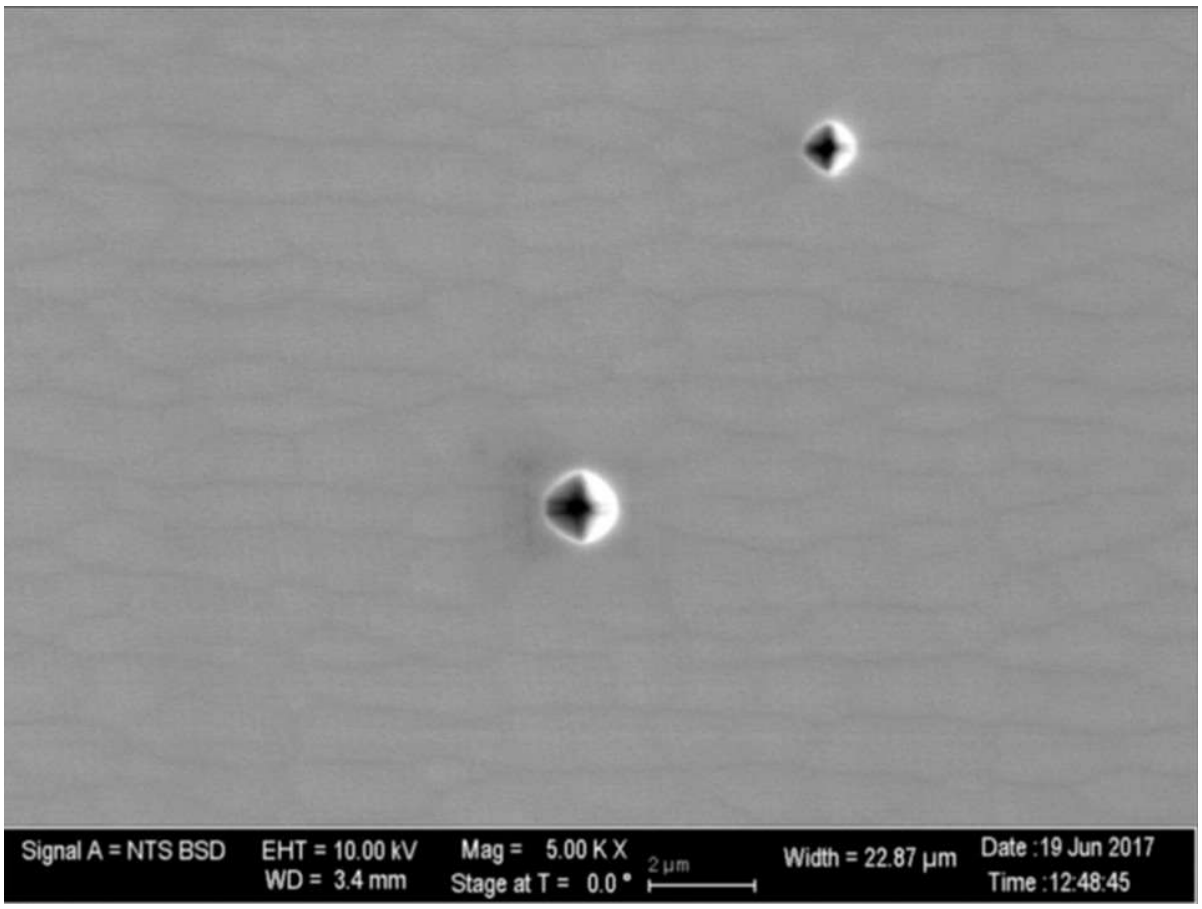

Figure 1.12: Picture of defect on M123 taken with Zeiss Neon SEM

We could think about the strain line as it is a backscattering image, but as these lines are also present in the AFM picture this is probably not what we are seeing.The other hypothesis is that these lines are created by elastic strain relaxation [23]. Additional clue in support of this hypothesis will be brought by later AFM measurement. This happens when the epilayer thickness is larger than the critical thickness for the given structure. Another set of sample has been later grown by the group and is shown figure 1.13. We could not find anything that looks like those defects but after playing with the brightness and contrast parameters on the image, we found those bounds. One could argue the growth condition for this set of structures are worst than before as the density of defect we see is larger on this picture than on the previous one (figure 1.12). But the smaller contrast indicates those defects are flatter than the one on the

previous set of samples.

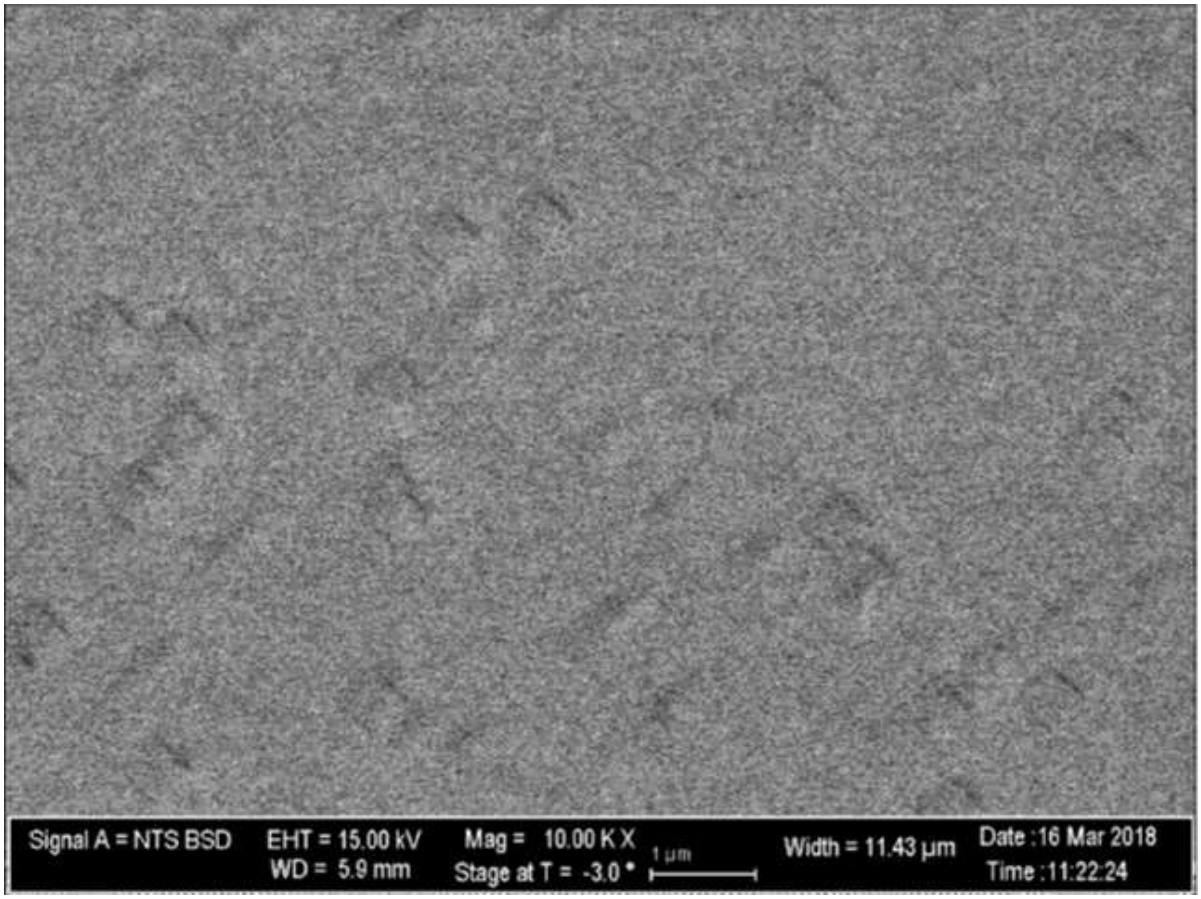

Figure 1.13: Picture of defect on M168 taken with Zeiss Neon SEM (Altered)

AFM measurements will show how different are those two set of sample and why we can say the later one has a better surface state. We also notice that we can not see the strain relaxation line anymore. This is because the mismatch coefficient is much smaller for this sample.

1.4.3 Backscattered electron image

Now that we know more about the defects shape and density, we continued our analysis of these materials by Electron Channeling Pattern which gives us information about the general crystalline orientation of the sample [22]. Then we used a diffraction technique called Electron Back Scatter Diffraction to get information about the orientation of specific spots.

Backscattered electrons can provide information on the crystal structure of the sample. There are different strategies that can be used to get crystalline information. One technique, Electron Channeling Pattern (ECP), uses the particle properties of electrons. Backscattered electrons are electrons from the incident beam that have been deflected with an angle over 90 degrees and we know that the probability of this happening is function of the distance between the incident electron and the nucleus of the atom [8]. In the case of crystalline materials, this distance will vary with the angle between the beam and the sample surface as we can see in figure 1.14.

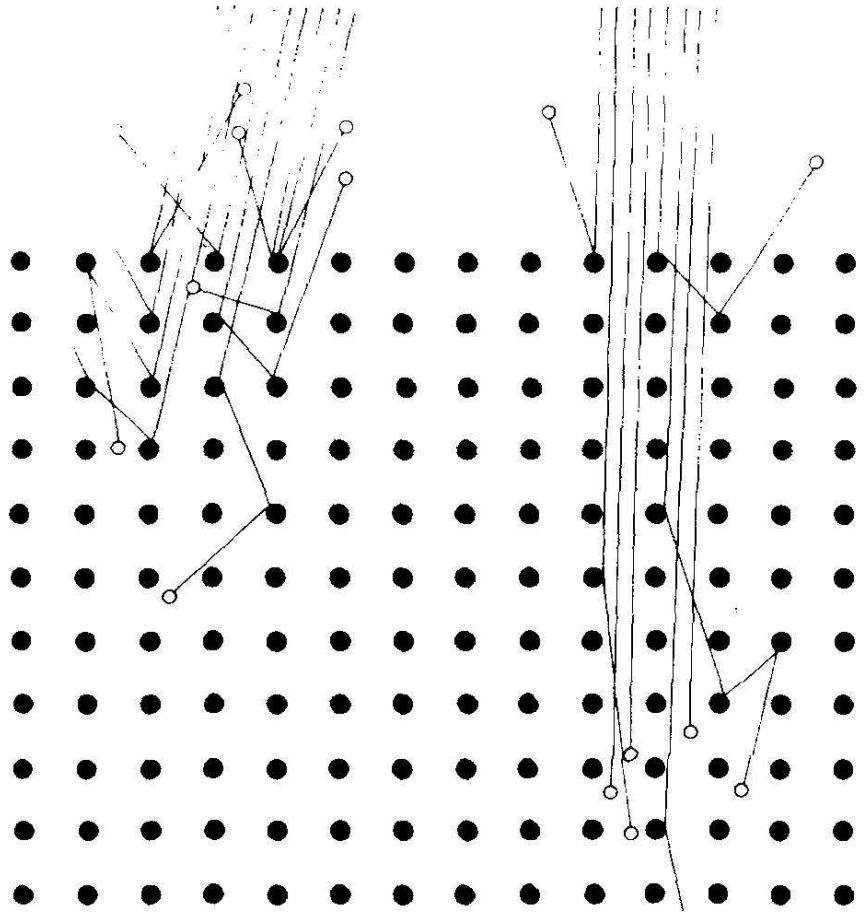

Figure 1.14: Electron Beam coming to a crystaline material at high (left) and low (right) incidence, [8]

The electrons on the left side of the figure arrive with a strong angle to the surface normal and are more likely to hit an atom near the surface. On the other hand, electrons with a small angle of incidence are more likely to continue into the material and scattered at high depths. They produce less detectable backscatter electrons than the ones with a stronger angle of incidence. The diffraction techniques use this matter of fact to identify the crystalline plane at specific spots. There are two different modes for this technique, Electron Channeling Pattern (ECP) where we scan the whole sample and Electron Back Scattered Diffraction (EBSD) where we scan it over a small area. First, let focus on ECP. In this configuration, we use the Backscattered detector of the Zeiss Neon which is located directly upper the sample. So, to maximize the signal, the sample is not tilted. This way the electrons beam comes with a normal incidence and most of the backscattered electron came back along the z-axis directly to the backscattered detector. Because of the nature of this technique, having a collimated incident electron beam is critical. We used an integrated function called high current mode which is a preconfigured lens setting that helps the collimation [24]. We want to proceed to an angular scan of the sample. The Zeiss Neon 40 does not have a module allowing to tilt the beam without changing its lateral position. But when operating at the lowest magnification, some fluctuation in the field of the coils used to direct the incoming electrons generate a slight rocking movement of the beam. We could use these data to determine the general crystalline orientation of the sample. But more importantly, by centering the electron channeling pattern, we can maximize the contrast on the picture obtained by the backscattering detector. Indeed, the dark area corresponds to the direction where fewer electrons are backscattered by the global crystalline orientation of the sample. If we center it, we minimize the number of detectable backscattered electrons generated by this specific crystalline orientation. So when the beam is over a defect, it encounters a surface with a different crystalline orientation and so, the number of backscattered electrons will differ. By making minimizing the amount of backscattered electron generated by the bulk orientation, we increase the crystalline orientation contrast. The practical way to minimize this signal is to center the ECP. It is done

by slightly tilting the sample. We proceed to this step before each session of imaging. The figure 1.15 shows the type of pattern obtain and the tilting we used to center it on the sample M129.

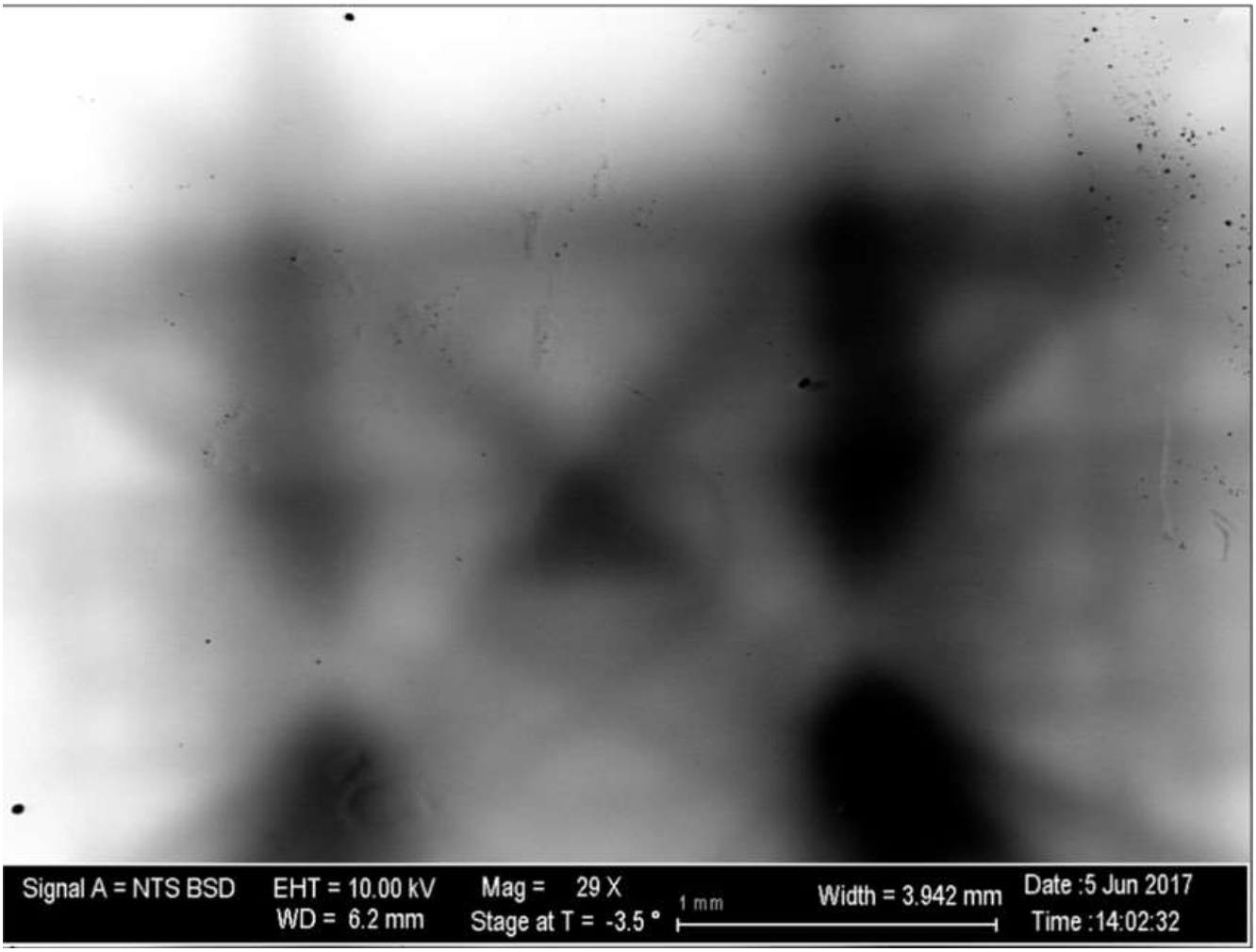

Figure 1.15: image of a centered Electron Channeling Pattern on M129

This pattern gives us the general crystalline orientation of the buffer. We want to study the defect orientation, so we also used EBSD maps of the sample surface at higher magnification. We imaged the sample at high magnification and obtained a diffraction pattern at each scanned spots. Then we can use these data to determine the local crystalline orientation of the defect. In this configuration, the sample is tilted at an angle of approximately 70 degrees to the electron incident beam as shown figure 1.16 [9].

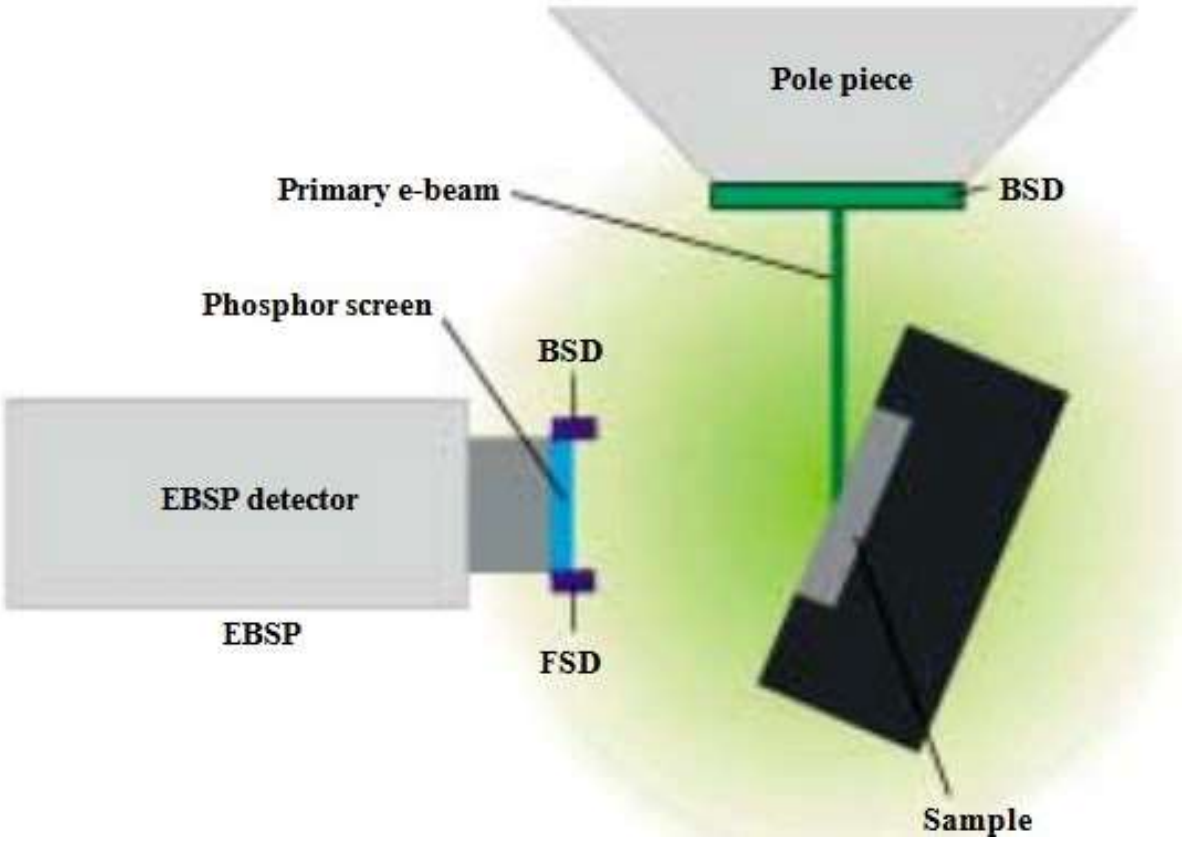

Figure 1.16: Scheme of an EBSD setup, [9]

The interaction between the electron beam and the sample will generate backscattered electrons represented by the green halo in figure 1.16 The Electron Back Scattered diffraction Pattern detector (EBSP) is on the side of the sample. So, to increase the number of backscattered electron received by the detector, we must tilt the sample. The beam will scan the whole designated area and return a diffraction pattern for each point. If there is a defect, the local crystalline alignment is affected by it and so is the distance at which the electron beam passes from the atoms. As a defect is more than a single atomic row in depth, it will also change the angle between the beam and the atomic row. We know that the condition to have diffraction is the Braggs condition 1.6.

$$2dsin(\theta) = n\lambda \tag{1.6}$$

As already said, the Braggs law gives the condition to have diffraction. Here n is the order of the

diffraction line, λ is the wavelength of the incident electron, d is the distance between atomic layers and θ is the angle of incidence of the beam. So, when the angle of incidence is changing, the diffraction pattern is changing too. We previously said that in the case of EBSD measurement, the electron beam is incident at a 70^o angle on the sample so the only way to change this angle is to have a change in the orientation of the sample surface. Regardless if we focus on the sample or a single defect orientation, to have useful data, we often have to increase the signal to noise ratio. The most common way to achieve this is to increase the aperture size letting more electron reach the sample. In the same time, we choose a high acceleration voltage. So, we get higher energy electrons which are more likely to be backscattered. There is also a high current mode on the acquisition software which needs to be activated to enhance again the signal to noise ratio.

data treatment

The software used for the post-processing treatment is provided by Oxford Instruments application and called AZtec. We want the crystalline orientation for each point. As the diffraction pattern is a function of the crystalline structure and orientation, the software can get the orientation from the EBSD pattern and the crystalline structure which is well known for the studied materials. An EBSD pattern is characterized by the lines which compose it. To identify the crystalline orientation, the software needs to know the direction of these lines. To digitize these directions, it applies the Hough algorithm shown on figure 1.17. We can see on figure 1.17 that the Hough transform identifies the intersections of the lines then indexes them. This algorithm is included in the software used for the EBSD data treatment. Two important parameters are the maximum number of lines per pattern and another parameter called the Hough resolution. In order to get more indexed points, we play with these two parameters but the data that we got weren't coherent with the physics. Indeed, due to a drift between the electron beam and the sample, these patterns are too poor. There is a mode integrated in the SEM acquisition software called drift compensation which balances this phenomenon by shifting the beam in the opposite direction of the

shif, but this was not activated.

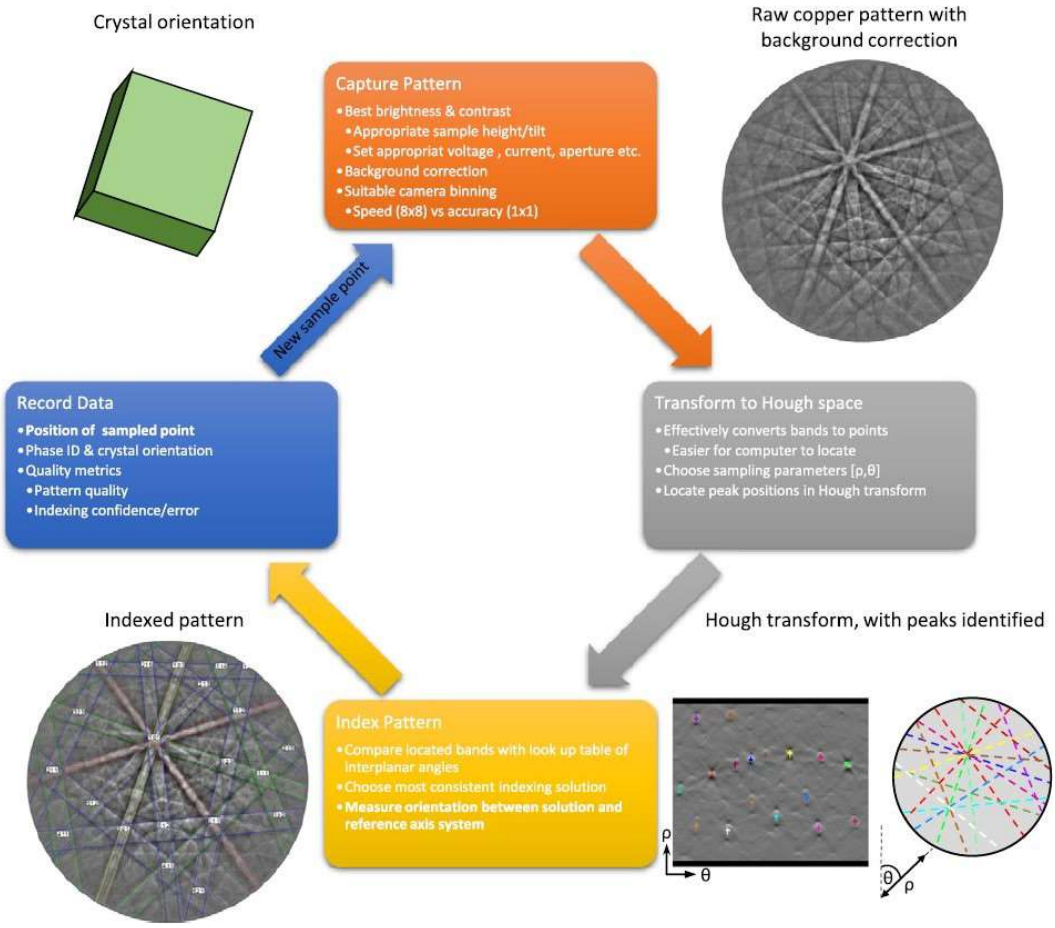

Figure 1.17: Hough algoritm, [10]

analysis

We took several EBSD maps of defects. Figure 1.18 shows the most complete pics we were able to get. We can distinguish different orientation on this figure. The red area corresponds to the orientation (0 0 1), the blue one to (1 1 1) which is coherent with the data collected in the section 1.4.2. The yellow spot reads (1 0 2). This spot does not make sense because the defect face should be along the (1 1 1) orientation. We investigated this anomaly and found it is an artifact caused by the beam shifting. To

make sure it was this, we asked the software to take a picture of the scanned area just before and after the EBSD acquisition. The beam shifting could be due to a charging or heating of the sample or other reasons.

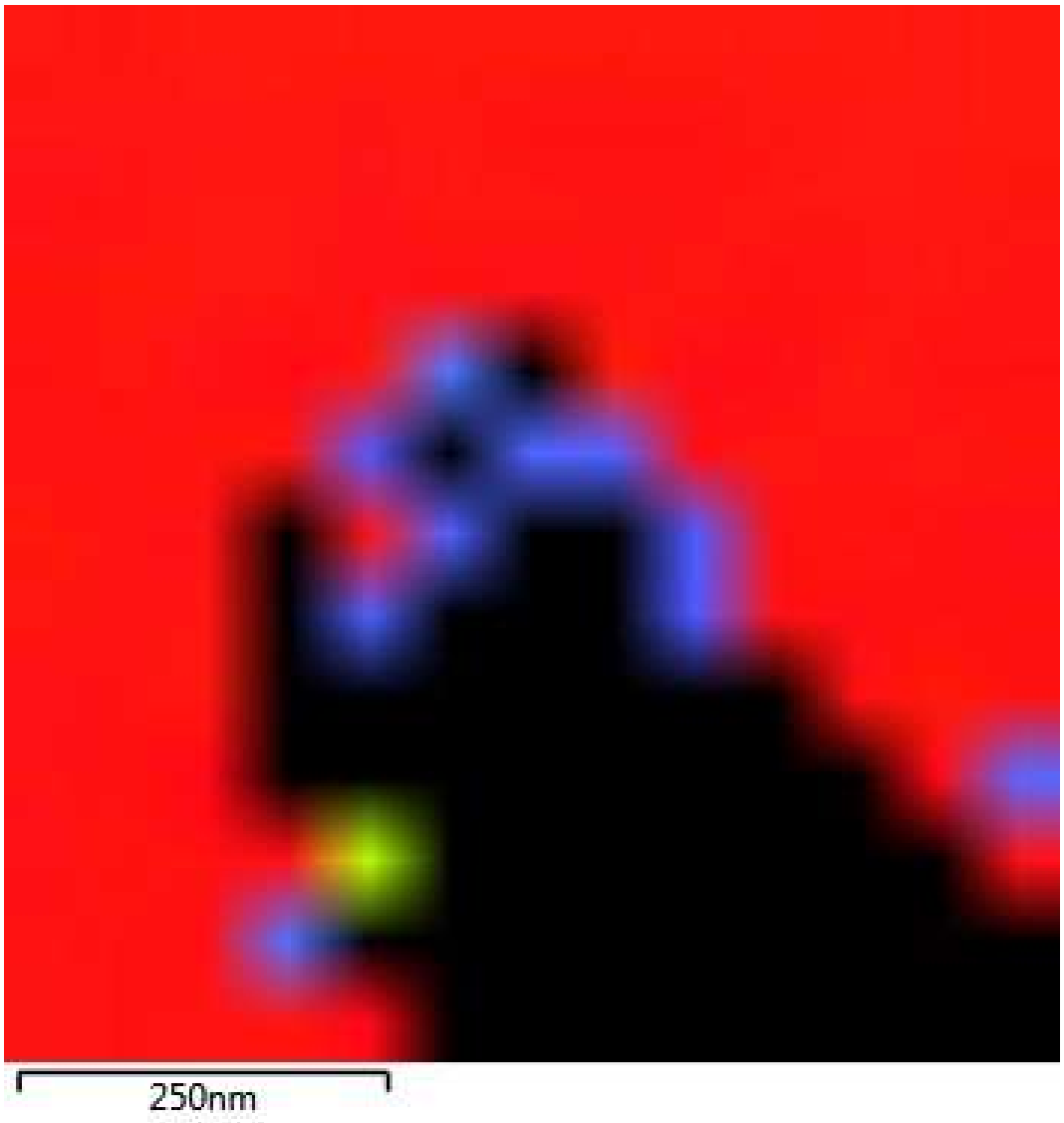

Figure 1.18: Map of the crystalline orientation of a defect on M126

We find that the area shift was in tens of nanometers. The spots in the blank area are the ones where the software couldnt identify the crystalline orientation. It is due to the poor signal over noise ratio as well as the drifting effect. We try to play with the scanning rate by either make it quicker to get less drifting

or by making it slower to increase the signal over noise ratio but it turns out that the configuration used to get this picture was the best we could reach. It could have been better if we were able to activate the drift compensation.

1.5 Atomic Force Microscopy

The last step of our analysis was the Atomic Force Microscopy which gives us information about the topography of the sample with a high precision. Particularly, the z or height sensitivity of these measurements allows us to detect surface feature flatter than a nanometer. Moreover, this technique is not sensitive to the stress changes in the lattice so we were able to determine that the line seen in the SEM pictures are physical changes in the surface and not stress lines. The con of using this technique is that it is more time-consuming.

1.5.1 Background

The Atomic Force Microscope (AFM) is a scanning technique which uses the atomic repulsive and attractive forces. It scans the sample at low altitude with a tip. The tip is pushed down by the cantilever and submitted to the interatomic potential and goes up and down in function of the local topography of the sample as shown figure 1.19. A laser beam is directed on the back of the tip and reflected to a photodetector array. As the tip is moving as a function of the interatomic potential and so the surface state of the sample, the laser is reflected to different areas of the detector. The detector used is divided into 4 quarters [25]. The software can get back the z position of the tip by making a ratio of each quarter response. There is two main mode of imaging in AFM [25]. We can work either in Contact mode or AC mode. The difference between those two modes can be spotted on figure 1.20. It is the distance between the tip and the atoms of the sample that define the regime. In the contact mode, the tip is actually very close to the atoms of the sample and can feel the repulsive force.

For the AC mode, the tip can feel the attractive and repulsive regime of the interatomic force [12]. During

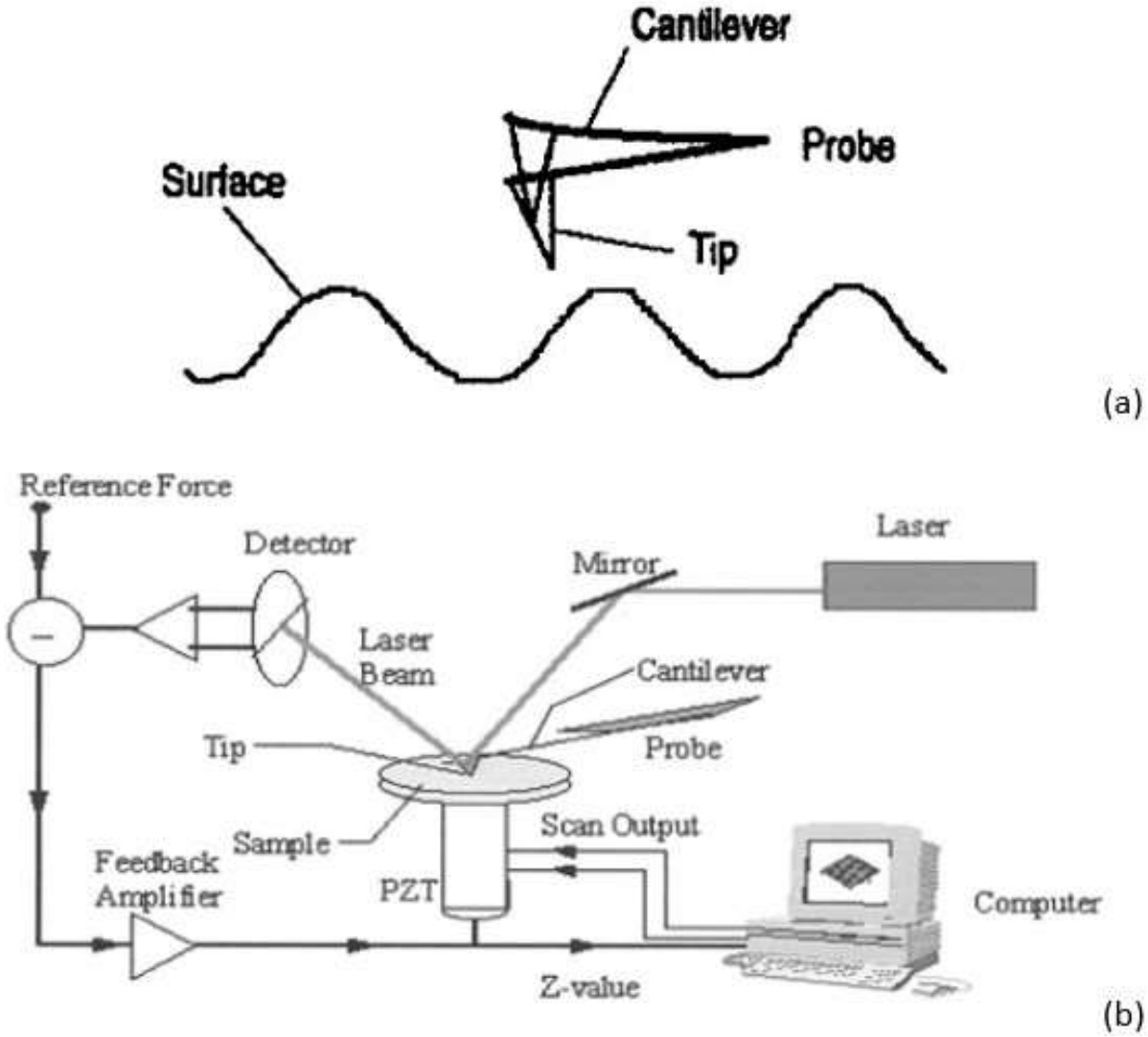

Figure 1.19: Atomic Force Microscopy Principle, [11]

this study, we only used AC mode, so the Contact mode won't be explained in this thesis. The AC mode uses the piezo actuator to make the cantilever oscillates at a rate just below its fundamental resonant frequency. In this mode, we want the oscillation constant in amplitude which requires a feedback loop. Indeed, when the tip is submitted to the interatomic potential, it will change its motion. As the amplitude of the oscillation is large (typically 100nm), the tip can be exposed to the two different regimes. Over the different interatomic forces, the prevailing one, and therefore the one involved in the change in position of the tip, is the Van Der Waals force. The feedback loop will change the input of the piezo actuator

and so the mechanical stimulation of the cantilever. We can use this feedback voltage as a measurement of the interatomic potential. Another option is to directly read the photodetector. In both cases, as the interatomic potential is linked to the surface topography [11], we can get back to this topography.

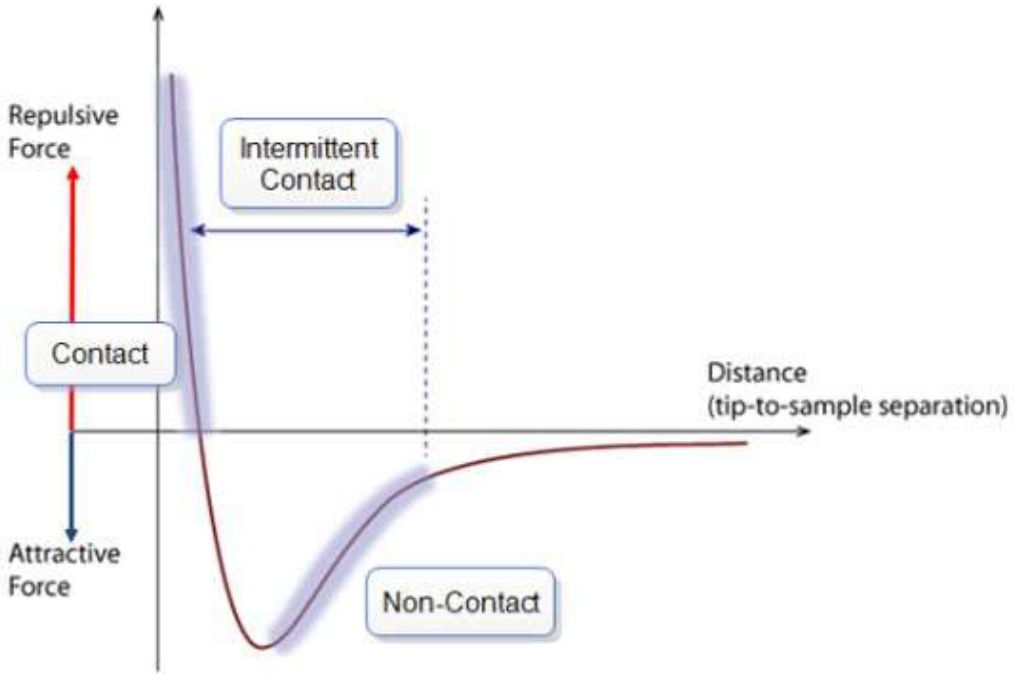

Figure 1.20: Interatomic Force in function of the distance between the tip and the atoms of the surface, [12]

1.5.2 Sample roughness

The surface of a semiconductor is not totally flat. Thanks to the law of thermodynamics and the fact we are not at 0°K there is always some fluctuation. The high z sensibility of the AFM technique allows us to measure it. The software used for treating the AFM measurement has a function for extracting the roughness of the surface along a line. We can set up the width of this line. To reduce the noise, we used the largest line possible while making sure there weren't any defect in the measured area. We took measurements on several areas of each sample and took the mean value. The results are reported in table 1.3.

Sample name	M126	M123	M127	M122	M129
Mismatch coefficient	$5.04 * 10^{-3}$	$4.45 * 10^{-3}$	$4.39 * 10^{-3}$	$3.94 * 10^{-3}$	$5.1 * 10^{-4}$
Roughness (RMS in nm)	0.68	0.63	0.53	0.51	0.38

Sample name	M171	M189
Mismatch coefficient	$4.2 * 10^{-4}$	$1.5 * 10^{-4}$
Roughness (RMS in nm)	0.19	0.16

Table 1.3: Roughness of the different samples

One can notice that when the mismatch coefficient goes down so does the roughness. It is coherent with the underlying physics. Indeed, if the difference in the lattice parameters of the two layer is smaller, the epilayer is less constrained and its deposition will occur in a more homogenous way. When the active layer has a high lattice mismatch coefficient with the substrate, its deposition will create defects and those bound we talked about it in the part 1.4.2). As noted before, the defect observed at the surface of the first set of samples are likely to be generated by strain relaxation. One of the strongest proof we got of this is the aspect of the samples surface we obtained by AFM[23].

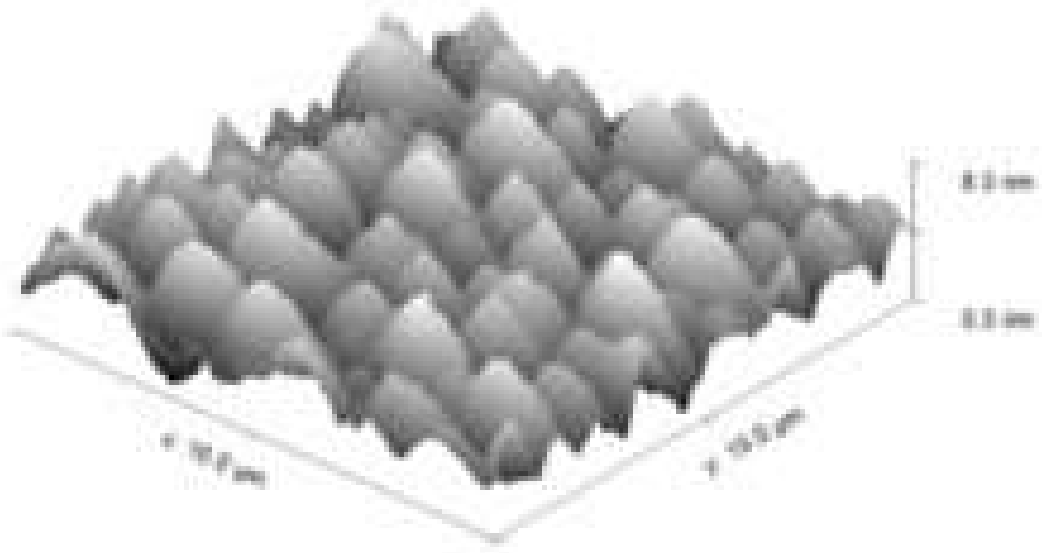

Figure 1.21: 3D view of the surface of M129 sample

One can see in figure 1.21 that there is vertical ripple at the surface. All the ripple are in the same orientation which is an effect of elastic strain relaxation.

1.5.3 Defect shape

We also used the AFM to image the defect on the surface of the samples. We used the software Gwyddion to analyze them. The original pictures that we got are presented in figure 1.22. The raw images are not contrasted enough to allow the characterization of the surface. We used the followed procedure to enhance the state of the pictures. We can see they were not contrasted enough to allow the analysis of these defect. The procedure that we used to enhance the pictures has been described as follows in the works of Cedric Corr*é*ge [2]

1. Align rows (using option matching)
2. Correct horizontal scar (using option stocks)
3. Level data to make facets point upward
4. Level data by mean subtraction
5. Remove polynomial background (3rd degree)
6. Shift minimum data value to zero
7. Blind tip approximation
8. Surface approximation.

The right picture of figure 1.22 is still not contrasted enough to characterize the defect and the strain relaxation lines. To obtain the best contrast we could with this set of picture, we used the local nonlinear edge detection module on Gwyddion. This edge detection increases the contrast of the image with a distorting the shape of the edge.

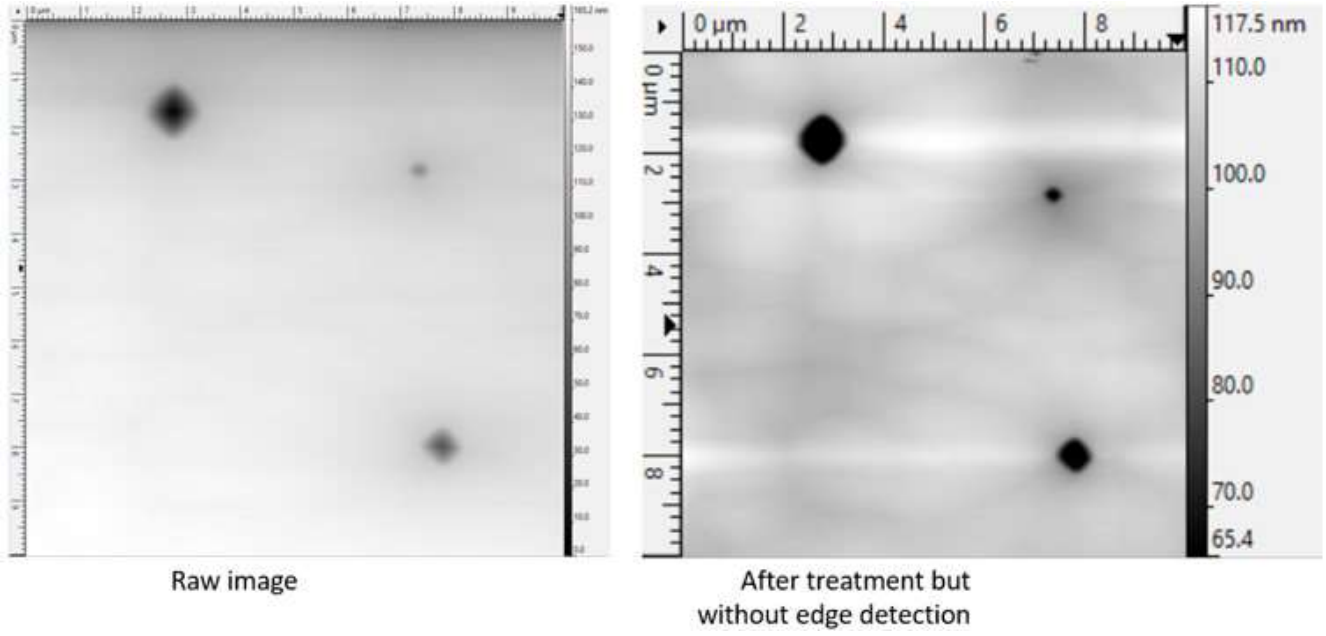

Figure 1.22: AFM view of the surface of M123 sample, raw picture on the left. enhanced picture (obtained by standard protocole [2]) on the right

We can see on figure 1.23 that the defects shape is changing slightly with the sample. A more noticeable point is that there is a cross on the top of the defect. One could interpret this as an artifact and can explain them by the abrupt change in the slope of the defect at its top. Indeed, when the tips reach the top of the defect, it passes from a (1 1 $\bar{1}$) plane to a (1 1 1) plane. The tip doesn't follow the change instantly but takes off from the surface of the sample for a short period of time creating this artifact. But by looking at the z-profile, we can also see this change along a vertical dimension. As this direction is normal to the scanning direction, those lines cannot be explained by this artifact. We investigated by taking a z-profile along a line at different x coordinate. The figure 1.24 presents a zoom done on M123 and the different z-profile we used to make our point. We didn't change its y position or its length. We notice there is a depletion before and after the defect. It occurs at the same y position as the anomaly we can see on it. One explanation could be there is a small defect at the surface of the sample at those particular y coordinates but the fact we etc see it and it is before the three different sample defect not at random place indicate us it is probably not what is happening here. We think it is a line of strain relaxation.

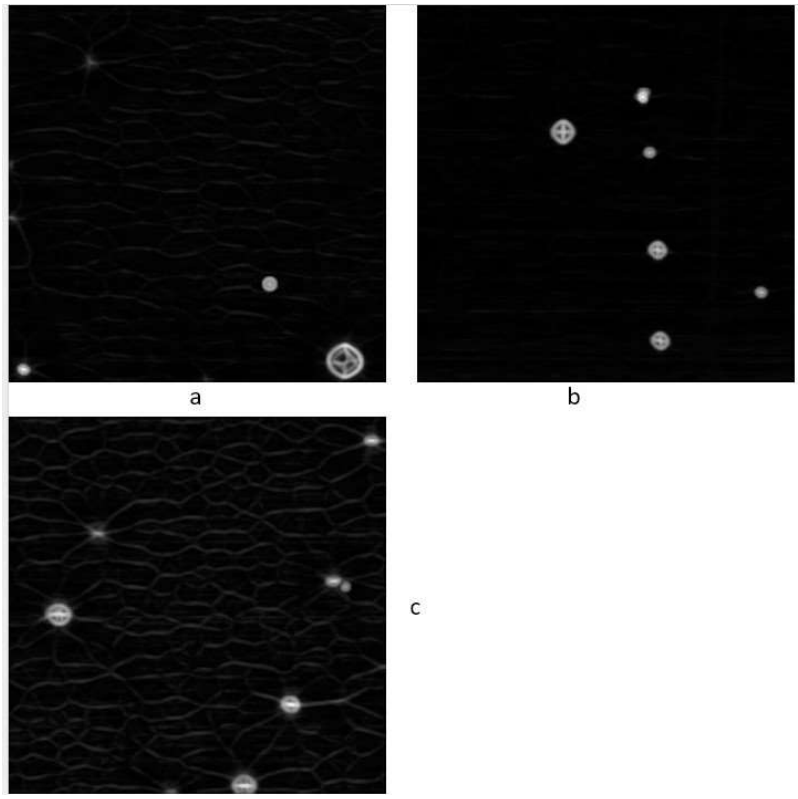

Figure 1.23: AFM View of different sample after treatment: a) M122, 31.7 times the critical thickness, mismatch coefficient: $3.94 * 10^{-3}$; b) M123, 36.9 times the critical thickness, mismatch coefficient: $4.45 * 10^{-3}$; c) M126, 43.1 times the critical thickness, mismatch coefficient: $5.04 * 10^{-3}$; All the picture have an area of $10 \mu m^2$

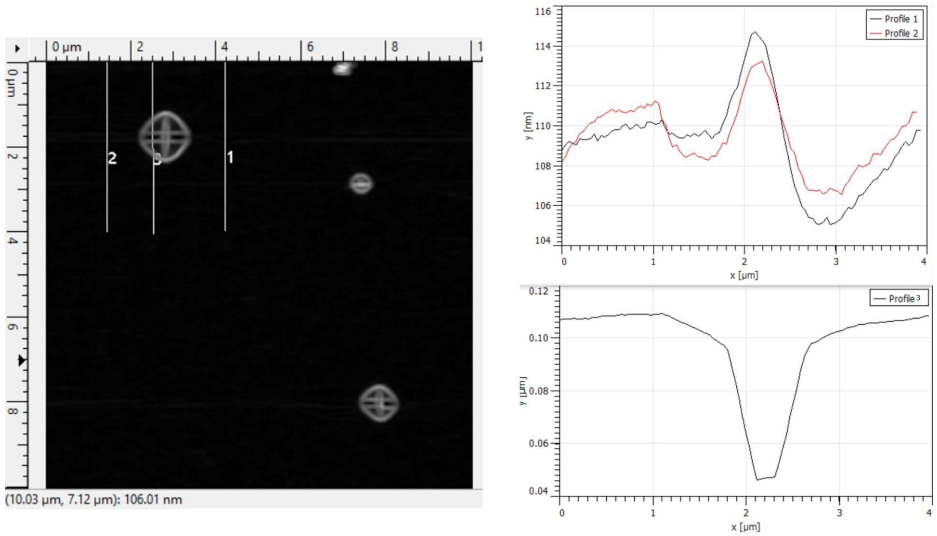

Figure 1.24: AFM picture of sample M123 and z-profile at strategic point

1.6 Conclusion

After DIC, AFM and SEM measurement on the different set of calibration structure, we notice a trend in the surface feature as a function of the mismatch coefficient as well as the ratio actual thickness to critical thickness of the epilayer. The table 1.4 show the defect density, the surface roughness and the general aspect of the surface for the different samples. It is important to notice that if the epilayer is

sample name	M126	M123	M127	M122	M129
x	0.154	0.024	0.145	0.031	0.078
Mismatch coefficient	5.04	4.45	4.39	3.94	0.51
$\frac{epilayerthickness}{criticalthickness}$	43.1	36.9	36.2	31.7	2.8
defect density($10^5.cm^{-3}$)	7.4	6.9	4.7	8.2	1.8
strain relaxation	++	++	++	++	+
roughness (RMS in nm)	0.68	0.63	0.53	0.51	0.38

(a)

sample name	M171	M189
x	0.0831	0.0885
Mismatch coefficient	0.42	0.15
$\frac{epilayerthickness}{criticalthickness}$	0.68	0.82
strain relaxation	Unseen	Unseen
roughness (RMS in nm)	0.19	0.16

(b)

Table 1.4: Surface features as a function of the mismatch coefficient and the ratio epilayer thickness to critical thickness for: (a): $GaAs_xSb_{1-x}$ over InAs structure; (b): $InAs_{1-x}Sb_x$ over GaSb structure

thinner than the critical thickness, we won't observe any strain relaxation line. The second point to get

from this study is that as the mismatch coefficient decreases, the surface of the structure get flattered and the concentration of surface defects decreases.

Chapter 2

Quantum well sample

In this chapter, we focus on Antimony Quantum Well (QW) structures grown on top of a GaAs or GaSb substrate. We expect the Sb QW layer to show a topological insulator behavior. Similar structures already have been grown but did not show this behavior, perhaps due in part to defects limiting the electron mobility. The objective here is to determine if any progress in the growth technique has been achieved by comparing the surface features of two structures.

2.1 Sample background

To understand the choice made in the structure, one needs to know that Sb behaves differently when in bulk or in a very thin layer. By nature, Sb is a semi-metal and therefore a good conductor. Nevertheless, when in a layer thinner than 7.8nm, Sb is predicted to behave like a topological insulator. Because of quantum confinement, only the surface is conductive [12]. First, we are going to review the carrier confinement achieved by quantum wells, then the mathematics basis behind the topological insulator. Finally, the notion of Hall effect will be briefly explained as it is the phenomenon we are trying to observe.

2.1.1 Quantum Well

A quantum well is an engineered configuration where we want to be as close as possible to the 1-Dimensional confinement textbook problem. It is obtained by MBE growth technology. A basic way to explain how this is obtained is that we alternatively grow two materials with a different conduction and valence band edge energy.

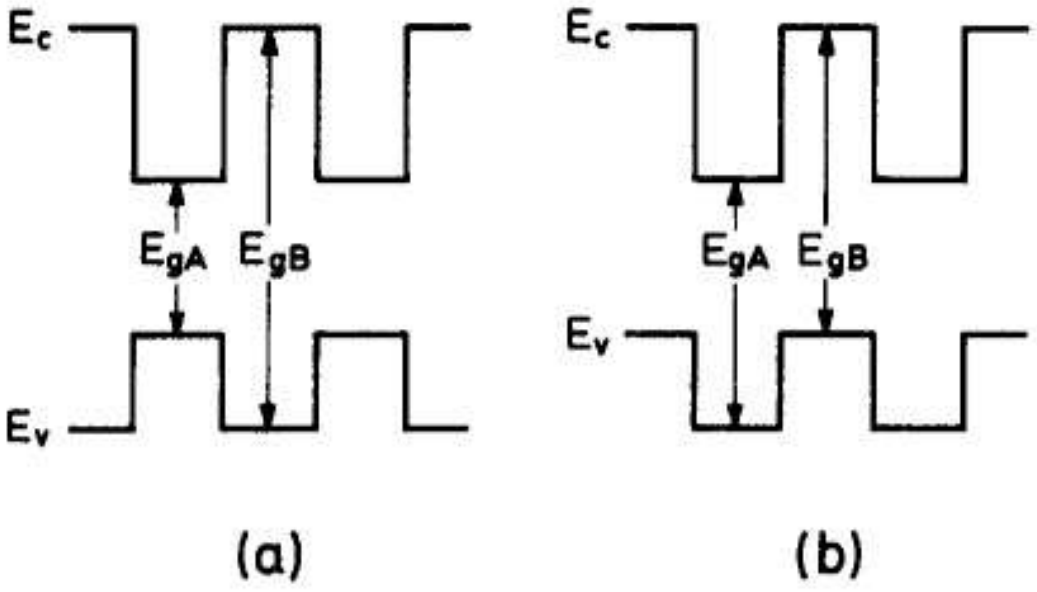

Figure 2.1: Band structure of a type I QW (a) and a type II QW (b), [13]

In figure 2.1 the energy of the edges of the conduction and valence bands are represented on the vertical axes. The horizontal axis is a geometrical dimension. We can see in figure 2.1 that there exist two types of QWs, the type I where the electrons and holes are trapped in the same physical space and the type II where they are trapped in two different regions. The type II QW makes the electron-hole recombination harder. As one can see on figure 2.1, the QWs obtained in the real world are finite potential wells and therefore differ from the basic infinite potential well where the solution can be solved by a simple formula. In our case, we need to resolve numerically the allowed energy level. More of them

are available when the physical dimension of the QW is increased as well as its depth. The physical dimension of the potential well has to be close to the de Broglie wavelength of the particle to show any quantum mechanics confinement of it[26]. If we consider an Sb layer with a varying thickness, the quantum confinement effect will shift the ground energy of its electrons[27] according to the equation 2.1.

$$\Delta E_B \sim \frac{1}{m^* L^2} \tag{2.1}$$

where m^* is the effective mass of the electron in the Sb layer, and L is the thickness of this layer. One can notice that this shift will become more and more important as the thickness of the Sb layer will keep decreasing. For Sb, the band structure is type-I, but with $E_g < 0$. Eventually, the quantum confinement is important enough for the ground state of the conduction band to be higher than that of the valence band. Only the electrons of the surface have a non-null conductivity and the structure is therefore a topological insulator. Let's now focus on the structure of the device. It is shown in figure 2.2. The difference between the two devices is in their composition so we put the two structures side by side. As we can see in figure 2.2, the device has been grown on top of a GaAs substrate along the plane (1 1 1). A buffer layer was required to grow the Sb with the lowest defect concentration. It is critical as this layer is where we expect the topological insulator behavior to occur. It means that the bulk should be non-conductive but the presence of defect can act as doping element and increase the conduction of this layer [12]. We do know that this phenomenon will occur but we want to minimized it.

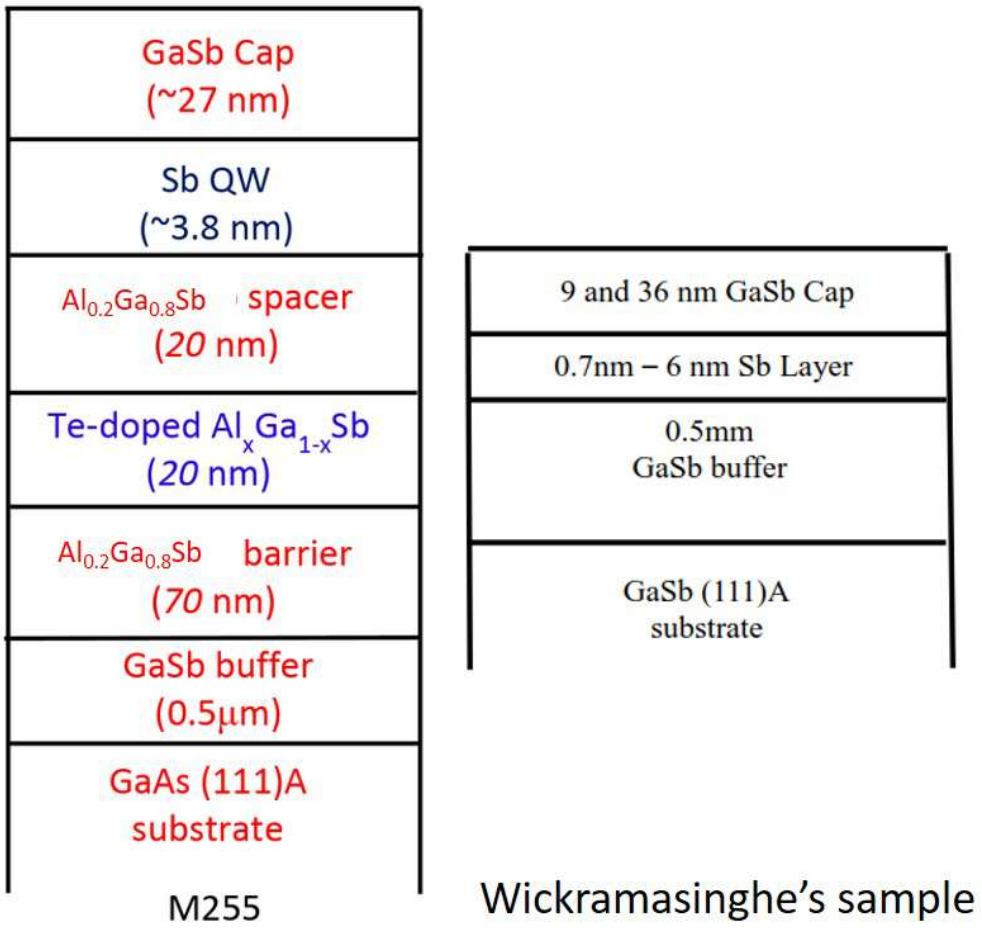

Figure 2.2: Structure of M255

2.1.2 Topological insulator

This set of samples has been grown to investigate the charge transport properties in Sb QW. As it has been said, at this particular thickness, Sb layer acts like a topological insulator. A topological insulator is a configuration where the valence band structure is topologically twisted or non-trivial [14]. By non-trivial topology, one must understand a topology without open set but the empty space and the whole space. Let's use an example to illustrate this notion. On figure 2.3, we can see that whatever z we use, we can always make a complete rotation without crossing any edge. It is what we call a global section. In the case of figure (b) though, only at z=0 can we do the whole rotation without crossing any edge. For any other z, a 2π rotation crosses the two edges. In this case, there is no global section but in z=0. The

set z∈]0;1[is open and therefore the bunble topology is non-trivial.

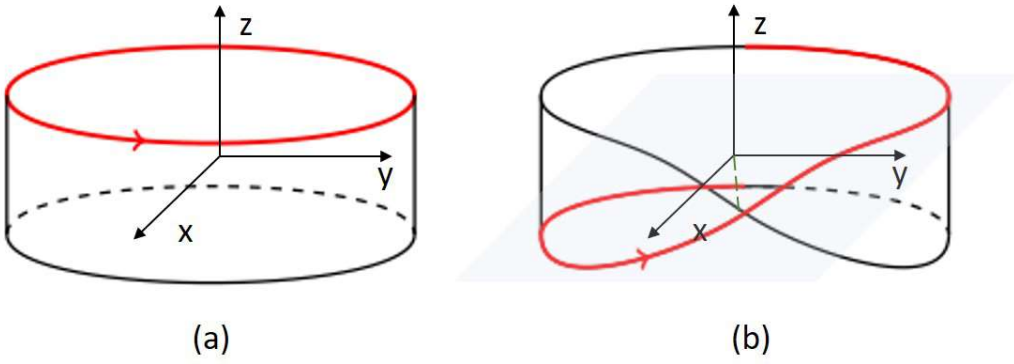

Figure 2.3: example of a trivial (a) and non-trivial topology bunble (b), [14]

A material with such a band structure will show a non null energy gap between its valence and conduction band everywhere but at is surface. So the surface has a band structure of a conductor while the bulk has an insulator ones.

2.1.3 Hall effect

The Hall effect has been discovered in the second half of the 19^{th} century. Dr. M. Santos group took Hall effect measurements on the sample to control its resistivity, carrier density, and mobility. The textbook case of Hall effect is a rectangular piece of conductive material. A magnetic field is applied in the orthogonal direction. An electric current is then established in the conductive piece. The moving charges in the magnetic field are submitted to the Lorentz force (2.2).

$$\vec{F} = q\vec{v} \times \vec{B} \tag{2.2}$$

Where q is the electric charge, $\vec{v}$ is the velocity of the charged particle and $\vec{B}$ is the applied magnetic field. One can see from the mathematical expression that the direction of the Lorentz force is normal to B and to v and therefore to the electric current. The magnetic field will push the charged particle in a

direction normal to electric current. They will eventually encounter the edge of the device and accumulate there. At a point, it will generate a high enough electric field (E) to balance with the magnetic force. In steady state, the voltage normal to the electric current direction is given by equation **??**.

$$|v| = \frac{IB}{ne} \tag{2.3}$$

where n is the density of electrons in the quantum well.

2.2 Defect analysis

Let's focus on the presence of defects and their shape. We expect to have fewer defects in quantity than the previously grown sample. So the surface of the sample should be smoother. It is also interesting to see if we can spot any change in the size of the defects.

2.2.1 SEM

The SEM has been used to image the sample in order to check the shape of the defect. As some previous tests were conducted on the sample to measure its conductivity, we had to clean the surface to remove any possible residue. This was done by rinsing it with acetone then isopropanol and finally deionized water. We then dried the sample with nitrogen gas and put it in the SEM. Several pictures have been taken. One can see in figure 2.4 the shape of a defect in the cap layer. One can notice that there are more defects on the old sample (figure 2.4.b) than on the newer one (M255) (2.4.a). Indeed, the field of view of the top figure is four times larger than the bottom one and still, we notice only one on the top picture instead of several on the second sample. But the defects on the old sample are smaller in area than the one we see on the new sample. The defect on M255 has an exterior side of 2.03μm and an internal of 0.96μm. The corresponding defects on the old sample are approximately 0.61μm. It is unexpected because usually larger defects are caused by worst growth conditions than the small ones. So

if we only see large defects, we expect to see more of them. It is not the case here and this result could be explained by the fact we are not looking at the same surface. The measurement on the old sample has been made directly on the Sb QW layer while the measurements on the newer one have been made on the cap layer.

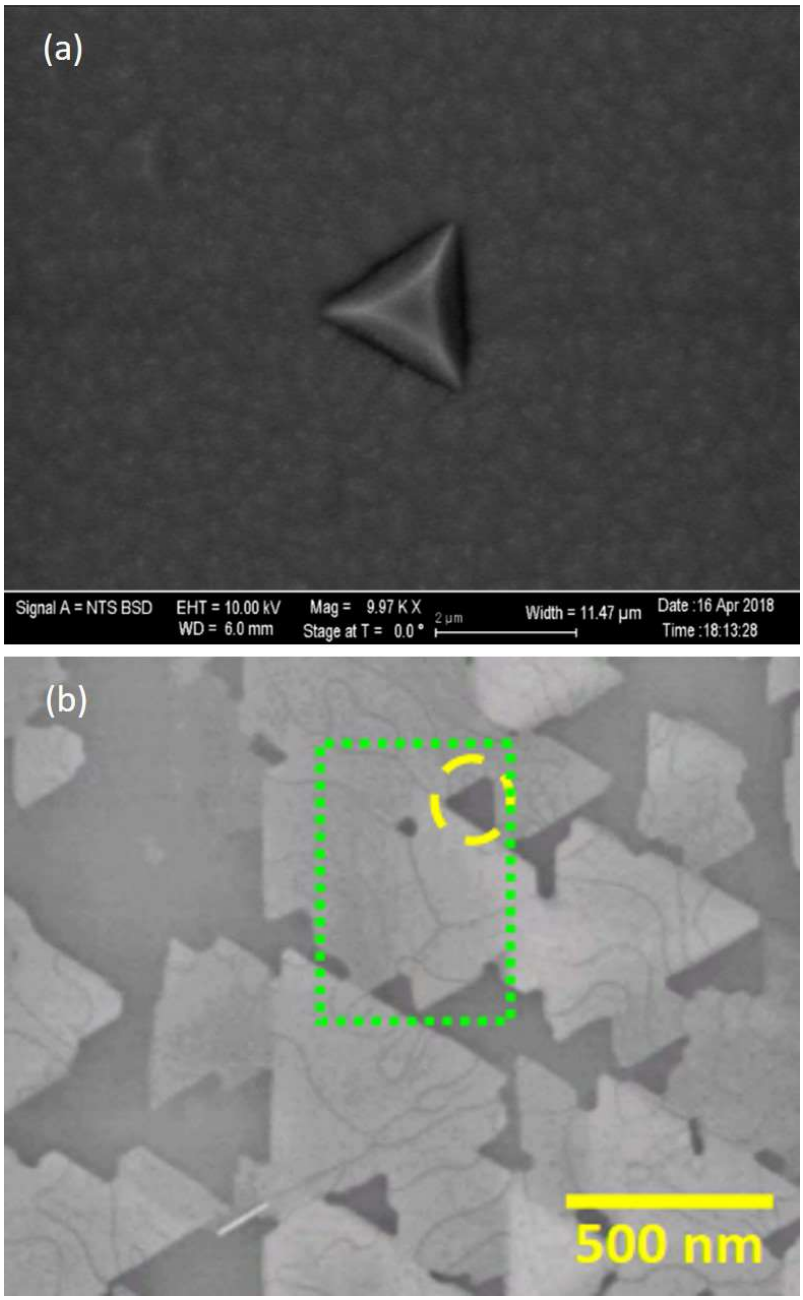

Figure 2.4: (a) SEM view of the defect in the cap layer of M255. (b) SEM view of the defects in the sample previously grown [12]

To be visible on this surface, a defect in the Sb QW layer has to be large enough to generate defect on the cap layer. It could explain why we can only see the large ones. The reason why we did not etch this cap layer to find ourselves in the same experimental condition is we had to save the sample for later electric measurements. As those need the whole structure, we could not damage it by removing its top layer.

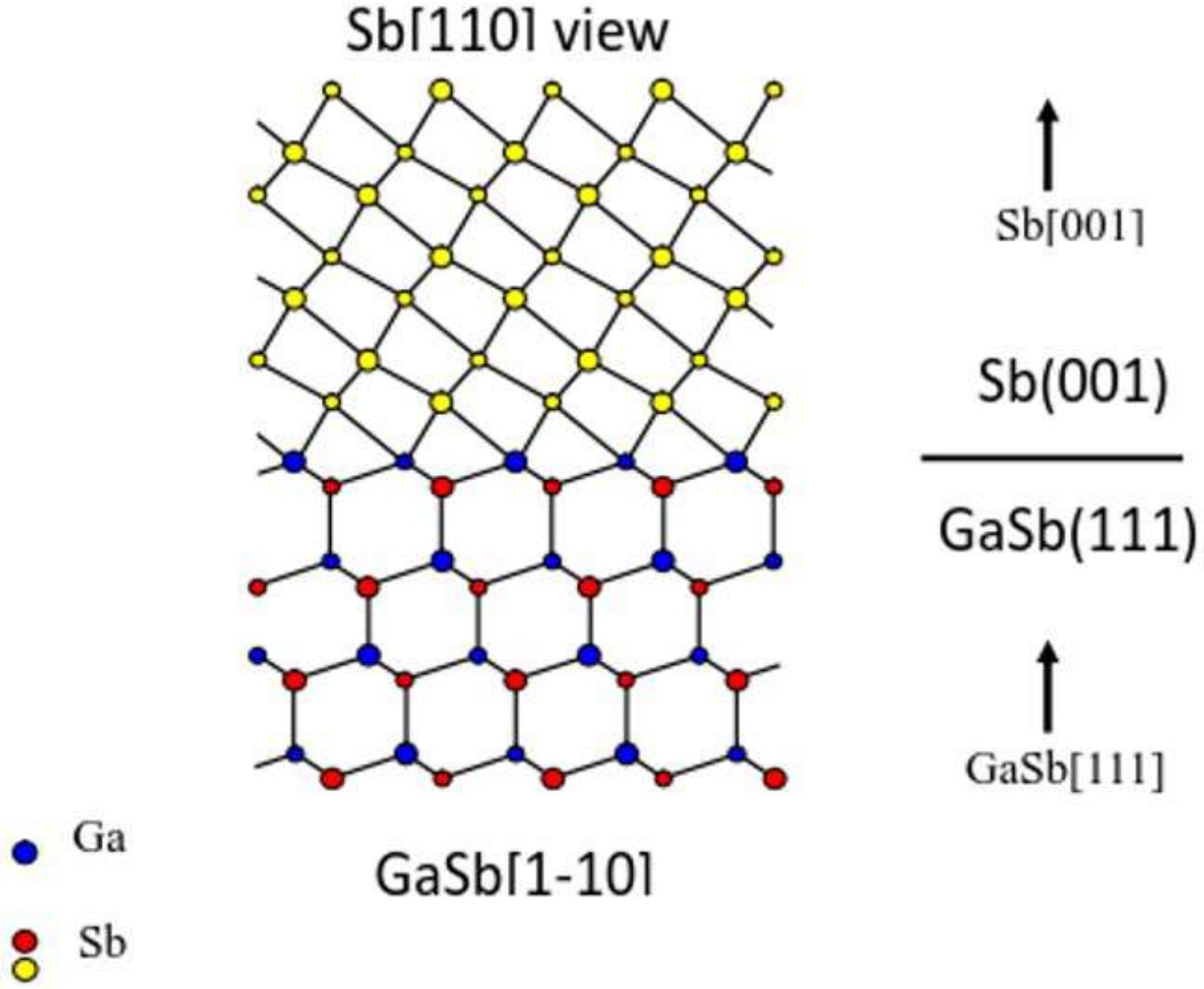

Figure 2.5: Crystal structure of the two different layers, from [12]

We can also spot a difference between the shape of these defects and the shape of the defects studied on the first part. Here, the defects are triangular. This is due to the crystalline structure of the materials.

GaSb has a Zinc-Blende crystal structure and is grown on top of a rhombohedral Sb structure. The zincblende lattice is an fcc lattice with a two atom basis. The (111) surface of an fcc lattice and the (001) surface of a rhombohedral lattice both have a hexagonal surface net. In the case of GaSb and Sb, the dimensions of the hexagonal surface nets are within about 0.1 %. Therefore, an Sb (001) layer is nearly lattice matched to a GaSb (111) layer. This alignment is shown on figure 2.5.

2.2.2 AFM

We are also interested in the roughness of the sample. Pictures have been taken in several areas and an average of the RMS roughness has been computed. The average value obtained is 2.5 nm. It was 1.25 nm on the ones grown by Wickramasinghe [12] which is the same order of magnitude.

Nevertheless, one can notice in figure 2.6 that M255 is dirtier than the previous one. It is due to Hall

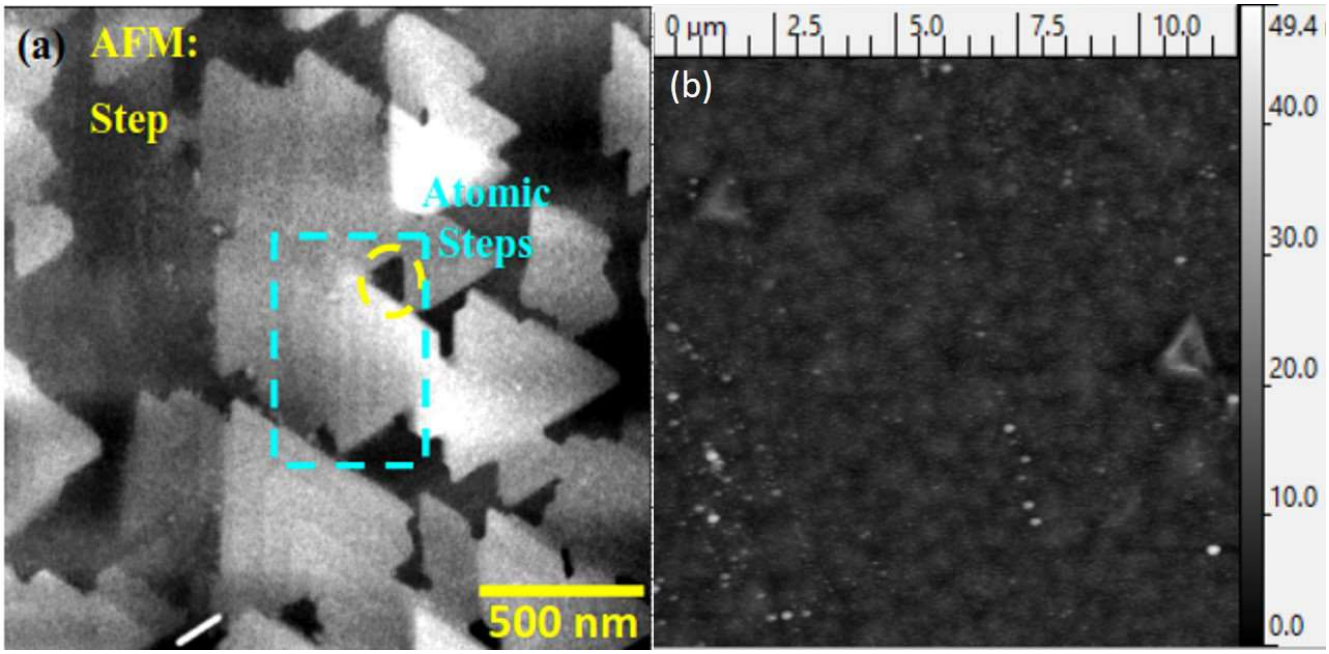

Figure 2.6: AFM view of: (a) Wickramasinghe's sample; (b) M255

effect test. Those tests have been conducted at different temperatures and the thermal cycle led to the formation of residue at the surface of the sample that we could not remove. Moreover, we did not observe the same layer in both samples. One can notice on figure 2.6 that there are much more defects on the

previously grown sample (a) than on the M255 (b). However, their flatness doesn't appear to decrease. We read from the height data that the defect on M255 (b) is 17 nm height and others have measured on the previous sample (a) a defect's height of 2.2 nm.

2.3 conclusion

Our objective for this series of measurement was to determine whether or not improvement has been achieved in the growth of those structures. But because we had to maintain the integrity of the sample for later experiments and reference purposes, we could not reproduce the experimental configuration in which the previous observation had been made. From the data we collected, we can say there are still defects in the structure even though their concentration seems smaller than before. Nevertheless, we cannot say anything about the relative quality of the sample as it appears we only see the large defect. So there is a possibility that smaller defects are in higher concentration and we can not see them because they are cover by the cap layer as well as the surface's contamination.

Part II

biological samples

Chapter 3

Strepsiptera eye

In this part, we investigate, in close collaboration with Marisano James, the eye structure of Strepsiptera. The goal was to provide a 3D dataset of it. It has been done by using the Zeiss Neon EsB 40 SEM. We operated the integrated focused ion beam to etch the sample without having to take it out of the vacuum environment. This part has been integrated to the thesis as a training for ion etching technology.

3.1 Introduction

Strepsiptera is an endoparasite which can be found in other insects such as a paper wasp [28]. By endoparasite, one must understand they live almost their whole life inside another living being. Actually, the female never exits its host. The male will leave its host at the end of his life to find a mate. It only has a few hours (approximately four hours) to do so before dying. It has some olfactory sensor to do the long-range search [29] but has to switch to optical searching once it gets close enough. Because of its short life expectancy, it needs to be really efficient in its search and therefore the optical vision system is highly developed. This part focused on the SEM study of the male individual Strepsiptera eye structure. First, we will develop the prerequisite step we had to complete before imaging the sample. Then we will see how we took the measurements and finally what conclusion can be drawn.

3.2 Sample preparation

As Strepsitera is a biological sample, we had to take care of some issues we did not have while imaging semiconductor samples. The first is the high z-contrast of the sample. Indeed, both FIB and SEM systems have a z-dependent focus so if the etched surface is too irregular, the etch speed will dramatically vary from one point to another. It is also true for the imaging where only a part of the image would be focused. The chosen solution to this problem was to encase the sample in a resin block. Another issue we had to resolve was that the eyes are small compared to the sample size. It is not problematic for an optical microscope as we have a certain focus depth and therefore can image even it is not really at the surface. But for the SEM, we can only image the true surface. To save time and the ion beam lifetime, we choose to use a microtome to cut the sample as close as possible for the eyes structures to be exposed. This way, the undetermined area we had to etch through to start seeing the eyes is smaller.

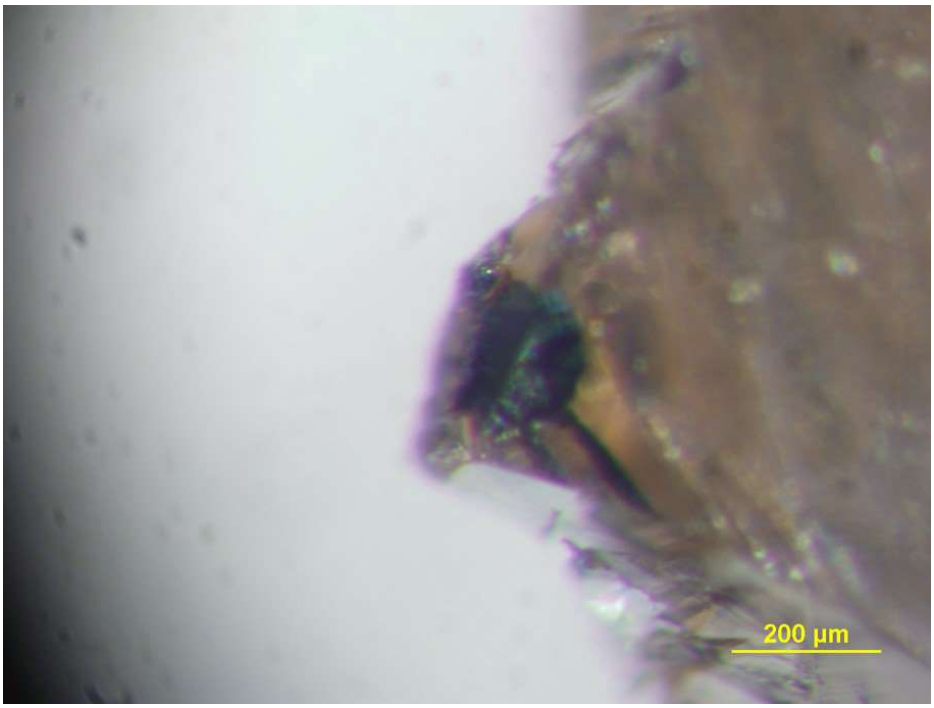

Figure 3.1: Optical view of the sample after cutting

At this time in the process, we captured some pictures of the sample with an optical microscope. The objective is to document the orientation of the Strepsoptera and the approximate position of the eye in the resin. Figure 3.1 is an optical microscope image showing the size of the sample. We can note that the eyes are on the bottom side of the tip. As the sample is composed of resin and biological material, it is susceptible to the charging effect commonly seen in insulating samples in the SEM [7]. To avoid this effect, a thin ($\sim$5nm) gold layer is sputter coated onto the surface of the sample. This layer will eventually be etched away by the focused ion beam during the images acquisition. But thank to the low incident electron beam current and the fact that some of the ions from the incident beam are implanted in the sample helps to reduce the charging effect. Sputter coating is a technique used in semiconductor manufacturing and electron microscopy preparation protocols. It is usually done in an argon atmosphere. A scheme of this process can be seen in the figure 3.2.

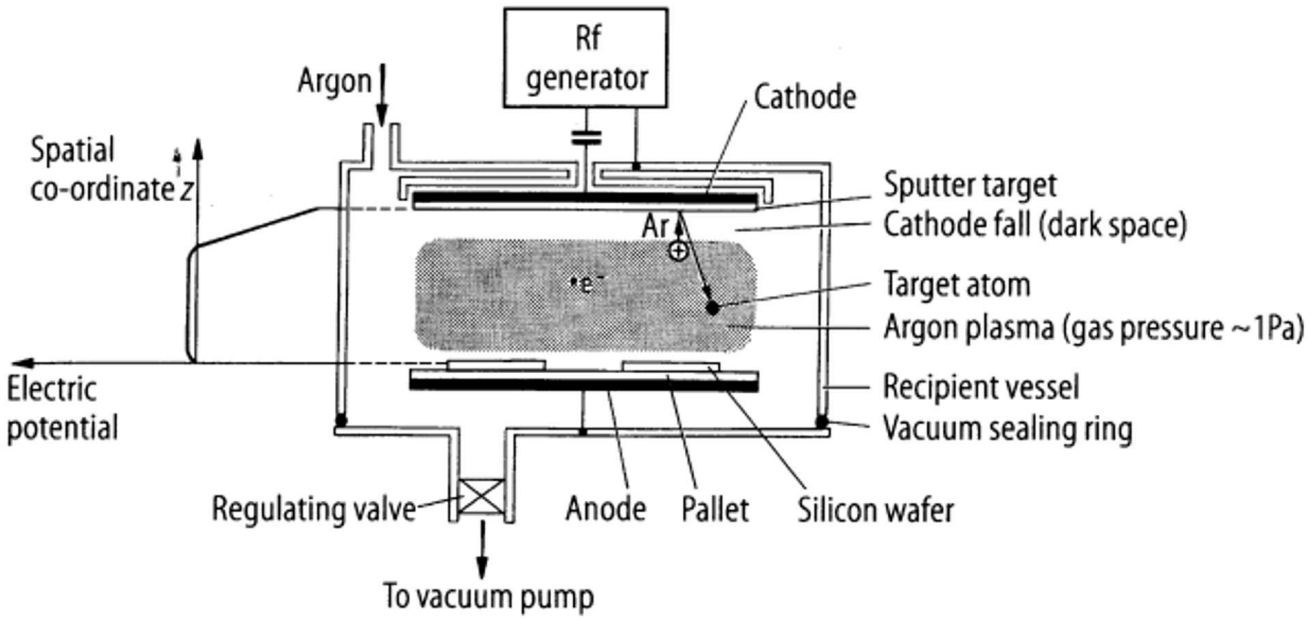

Figure 3.2: Principle of sputter coating, [15]

An applied electric field ionizes the argon gas and drives the ion particles toward the surface of a solid piece of material to be deposited. We will refer to this piece as the target. When the ions hit the target,

some atoms are ejected from it in random directions. Some of these atoms eventually reach the sample to be coated and attach themselves to it. Once those steps have been completed, we can put the sample inside the SEM chamber and start imaging.

3.3 Imaging

Once we put the sample inside the chamber, we can only see the surface of it. We did the microscope alignment on the resin and, with the help of the image from the optical microscope, start the etching in the region where we thought the eye was.

3.3.1 Focused Ion Beam etching background

The Zeiss Neon at OU has a Focused Ion Beam integrated with its structure. This element uses a liquid-metal ion source which is the most focused and the brightest ion source available with a ion beam size of $\sim$ 5nm [30]. We previously said the source is Gallium ion. It is because Ga has several interesting characteristics such as its low melting temperature and the fact it does not interact with W. So it won't attach itself to the structure of the ion gun. All those characteristic makes its flux one of the more stable when compared to other elements. Another reason for this material choose is that the Ga ion is heavy and therefore efficient in the etching of samples. Indeed, thanks to its mass, it has an higher kinetic energy than other atoms and can easily achieve substrate sputtering [17]. As one can see from figure 3.3, the directional beam is obtained by a strong electric field, up to $10^{10} V.m^{-1}$, applied between the Ga reservoir and the extractor. The condenser and objective are electromagnetic lenses and it is with them that one focuses the ion beam onto the sample. The apertures are here to define the size of the beam and their setup is stable enough to do adjustment only once a month, although, they are directly exposed to the ion beam and therefore will be milled over time. When this happens, the beam is not fully circular anymore and so the etching is less even. The Blanker plates are used as an ON/OFF switch. That serves to deflect

the beam off the sample [30].

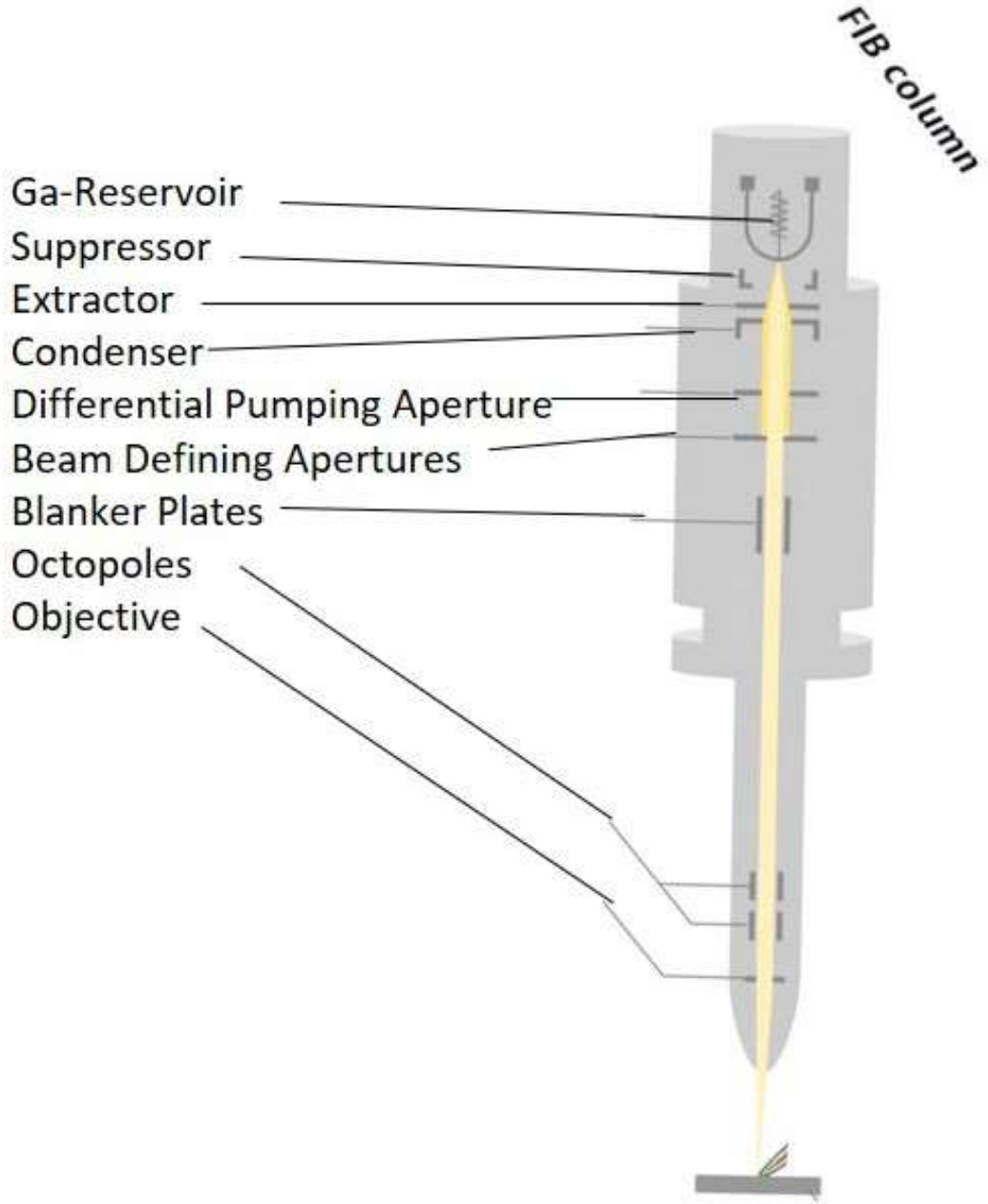

Figure 3.3: Principle of Liquid Metal Ion Source Focused Ion Beam gun, Model design by ZEISS, from [16]

The octopoles coils act as a stigmator and help keep the beam as circular as possible. To guarantee the stability of the beam, the manufacturer has established a lifetime below which the stability of the beam is uncertain. All the data we acquired were in a situation where we overpassed this limit. Nevertheless, the

etching seemed uniform. One of the consequences though was we had to operate with lower beam current (10 nA). The FIB interacts with the sample and generate secondary electron as well as secondary ion [30]. So, we can use the SE produced by the FIB to image the sample. When used in this configuration, it works as the SEM. Because we are not using electrons but ions, we have to use low current to not damage the sample. The images we took were at 2nA and even then, the sample was slightly etched while taking the picture. The reason why we did this is because we want a view from the FIB axis. It helped us to make sure the sample was really normal to the ion beam.

3.3.2 Image acquisition

The process of etching, stopping, taking a picture and return to etching without taking the sample out of the SEM is called slice and view. We want the beam to etch the sample evenly so we can see all the slice that interest us. Indeed, if it is etched with an angle, one part of the sample will be etched faster than the other. So, we will miss some part of it. The configuration of the SEM tells us that there is a 54° angle between the FIB and the SEM column. So we have to tilt the sample at this angle to get close to the normal FIB exposure. This said, there is two different possible configuration and we used both of them. The first we used is a situation where the region of interest is below the surface and the FIB etched plane by plane along the z-axis. In this case, we used the optical microscope to localize the targeted region and then directly etched a square in the bulk. The figure 3.4.a) show us this configuration. Another configuration, widely used as shown in the figure 3.4.b), is to have the FIB etching along the x-axis. We can see on figure 3.4.b) the presence of a thin platinum layer. It is there to prevent the formation of vertical etching artifact on the surface of the specimen while etching by making the surface of incidence of the FIB flat enough. The main difference between those two configurations is the orientation of the etching. In the first one, we have a sequence of horizontal views of the sample while in the second, the slices are vertical. One can see in figure 3.4.b) that this configuration requires a trench to be etched in front of the region of interest. This configuration will be documented with additional detail when we will

explain the detailed view of the eyelets.

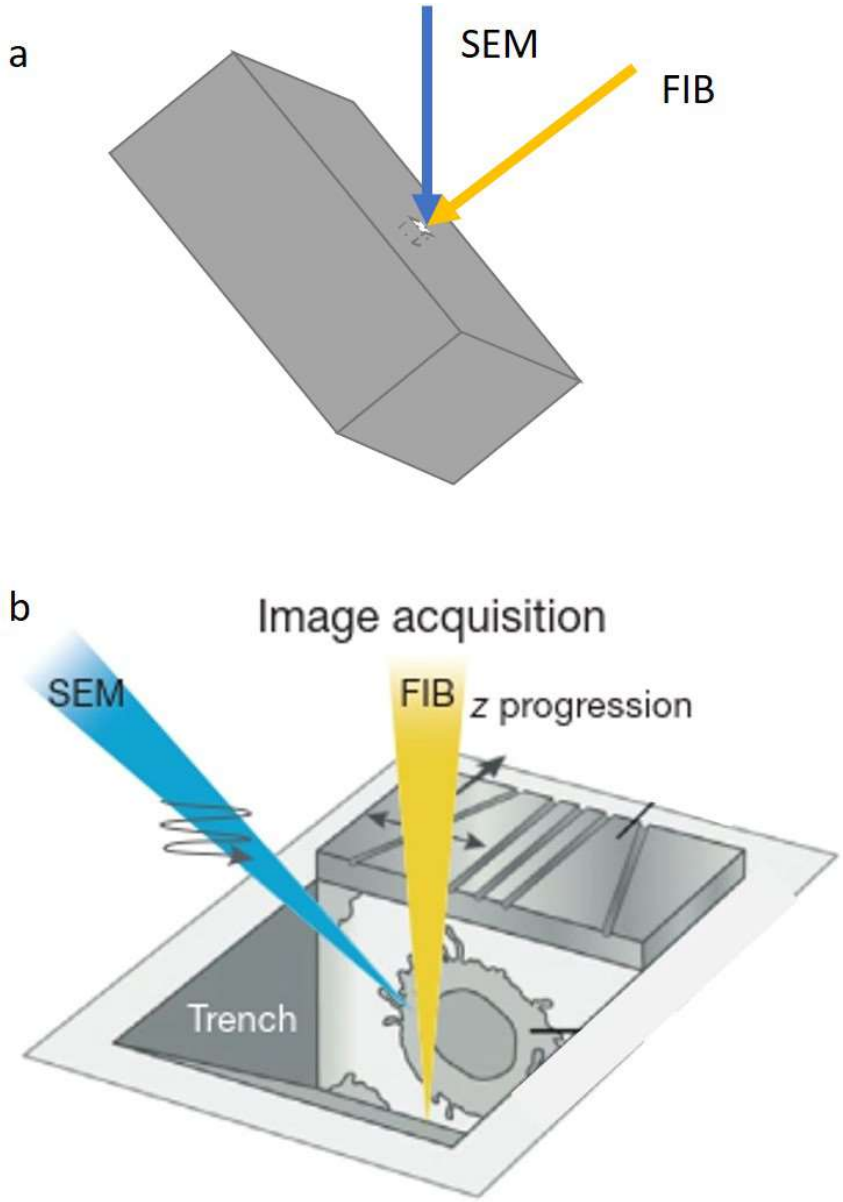

Figure 3.4: slice and view configurations: (a): Region of interest in the bulk, (b): Standard method to image region of interest in surface[17]

This is the main requirement for this configuration. But one of the reasons explaining why we used this technique over the first one 3.4.a) is the fact that we are sure of the perpendicularity of the sample surface with the ion beam. Indeed, in the first configuration, the sample surface can form a nonnull angle

with its support. So, we had to use the FIB imaging mode to make sure it was really normal to the ion beam. This mode of imaging required to have the electron beam and ion beam at the same point on the sample to be able to image where we etched. This point is called the coincidence point [17]. We first find the region of interest with the SEM, then we used the stage control to center it in the FIB view. We switched back to the SEM view and using the electron beam shifts, we made sure the region of interest was centered. We operate at a large working distance to be sure not to hit anything while searching for the coincidence point. As we are working with an important sample tilt, the first thing to do is to correct for the tilt eucentricity. Indeed, when we tilt the sample, the scanned region moves across the sample. We can correct it by changing the M coordinate which corresponds to the axis normal to the stage as we can see in figure 3.5.

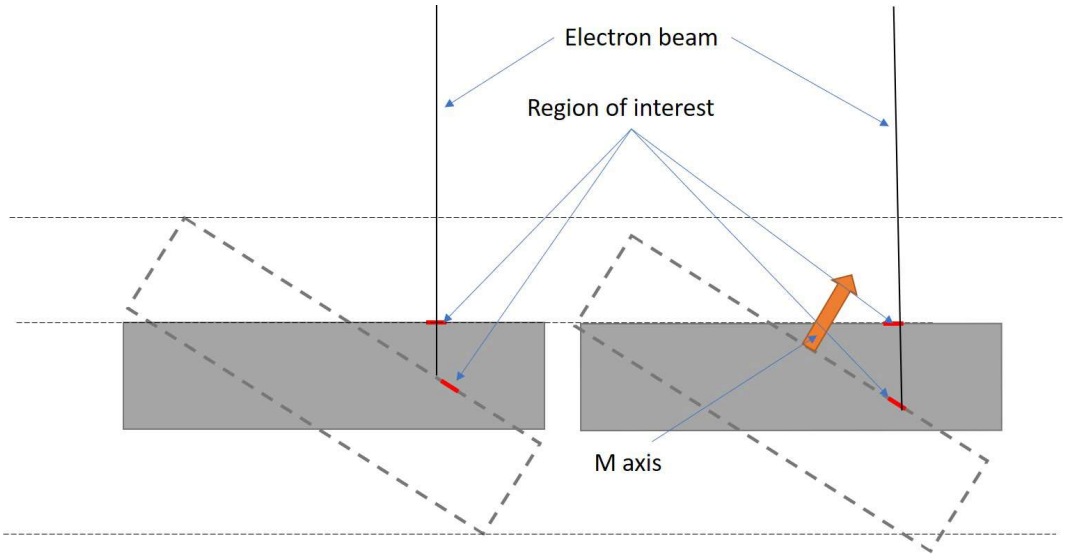

Figure 3.5: slice and view configuration

Once we have completed all these steps, we can proceed to the actual data acquisition. For time-saving purposes, we acquired images with the SEM without using the line integral and at a scan speed of 8 ($1.29 * 10^{-5}$ s per point) which return a good enough signal to noise ratio. For data treatment issues, we want the voxel to be the same size in all dimensions. So we made sure the lateral x and y pixel size was

close enough to the etching step value which essentially serves as the third dimension voxel size.

3.3.3 Analysis

Whole eye structure

The first set of data we acquired was a low voxel resolution image but covering the whole eye. We were in the configuration as described in figure 3.4.a). We used a fast etching setup with a FIB beam current of 10nA.

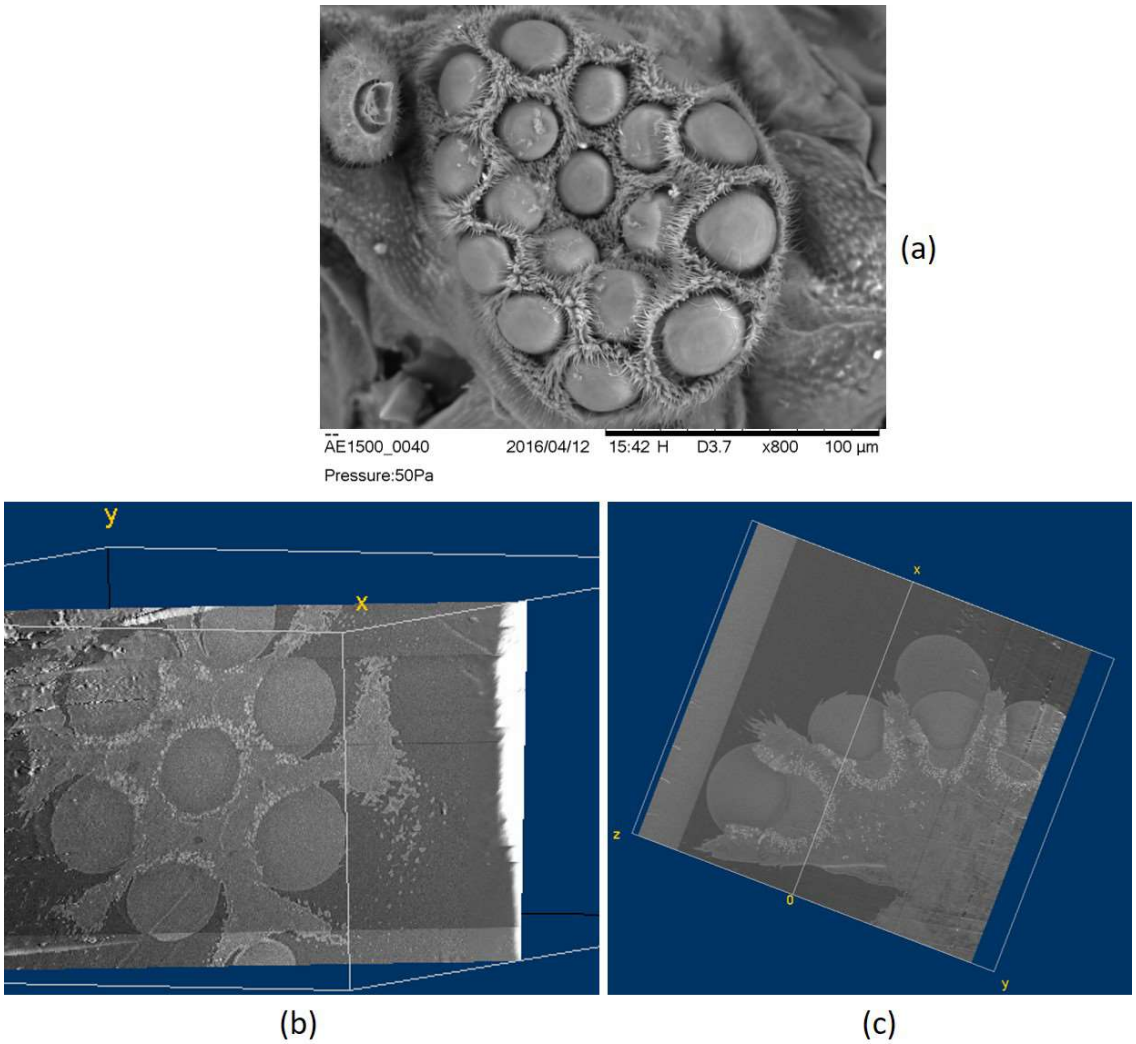

Figure 3.6: a): SEM view of an unbedded Strepsiptera eye taken by J. Marisano, b) top view of resin bedded Strepsiptera eye, c) side view of resin bedded Strepsiptera eye

We were able to get through the whole eye in a reasonable time (30 hours) doing this. Once we got the data, we open them as an image sequence in ImageJ. After cropping the pictures and passing them using the 3D plugin, we selected those views. The picture 3.6.a) is a view of an unbedded Strepsiptera taken by Marisano James. It gives us information about the global structure of an eye. We can see there is one central eyelet surrounded by an inner ring of six eyelets itself surrounded by an outer ring of eleven eyelets. The views are shown in figure 3.6.b and c are extracted from the tomography data. We put those data into Image J creating a picture stack we could turn and change the depth to get basically any view we want. So we could extract a top view and a side view. By zooming into the top view, we notice the presence of two different elements, one is rounded and work as a photodetector, the other is stretched and has a function of a reflector. We think it is used by the insect to increase the level of photons it can collect in a dark environment and maybe also to protect its eyes during bright day light. Indeed, this insect doesn't have any eyelid. The side view gives us information about the curvature of the eye itself.

detailed view of a eyelet

Once we got the data of the whole eye, we decided a high-resolution data set for a single eyelet would be interesting to learn more about its structure. Indeed, in the first set of data, the step between the two views is 500 nm. It does not seem too large but when we know the diameter of the whole eyelet is about 60 μm which means that there are only 120 data points to go through the eyelet [28]. Because it is already standardized and it allows to select precisely the scan area, we decided to use the second method, the one described in [17] and presented in section 3.3.2. To do the pre-etching, we used an ion milling current of 10 nA, then a fine current of 500 pA to reduce the formation of vertical etching artifact. Figure 3.7 shows the situation of imaging just before we started the slice and view process. We can see in figure 3.7.b that there are three different eyelets exposed. We aimed for the central top one which is one from the inner ring. The two other eyelets are from the outer ring.

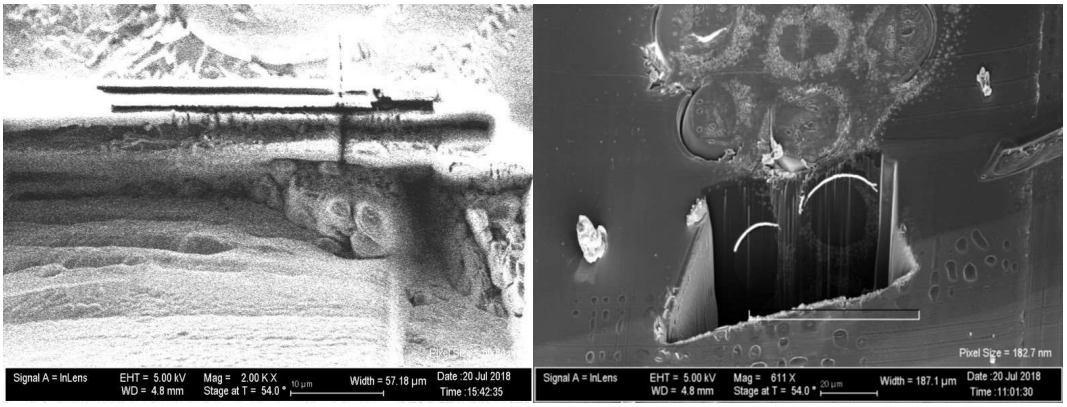

Figure 3.7: Different view of the setup for the tomography of a single eyelet: (a): FIB View; (b): SEM View with tilt correction

Figure 3.8 shows a high-resolution image of an eyelet from the inner ring. Figure 3.8.a has been taken on the top of the eyelet (i.e close to the middle of it). One can see that at this level, it is composed, almost exclusively of round small items. These are pigments and have an average area of 7.5 μm^2. We acquired this value by using the particle analysis module included in Image J. We used the Shanbhag color threshold method which gave a more accurate result. Figure 3.8.b and c have been taken more deeply into the eyelet. We can notice that some stretched items appeared. Those are also pigments and have a reflector function to allow the Strepsitera to increase the luminosity of its environment. It may also have a protective function. Indeed, this species doesn't have eyelids and therefore can't control the amount of light reaching into its eyes. But as it has such a small life expectancy, it may not require any eye protection. One can notice they are smaller than the round ones with an average area of 4.4μm^2. The view shown in figure 3.8.d is one of the deepest available in the measurement set. We can see that the eyelet is not closed yet. It means that we have not yet reached the actual photodetectors which are located below the reflector pigments [28]. It is due to the fact that we limited the etching to a maximal depth of 30μm for reliability issues. One can notice in figure 3.8 the presence of a trench in the top left side. It is due to too high milling current used for the initial milling of the trapezoidal shape in front of the main milling area.

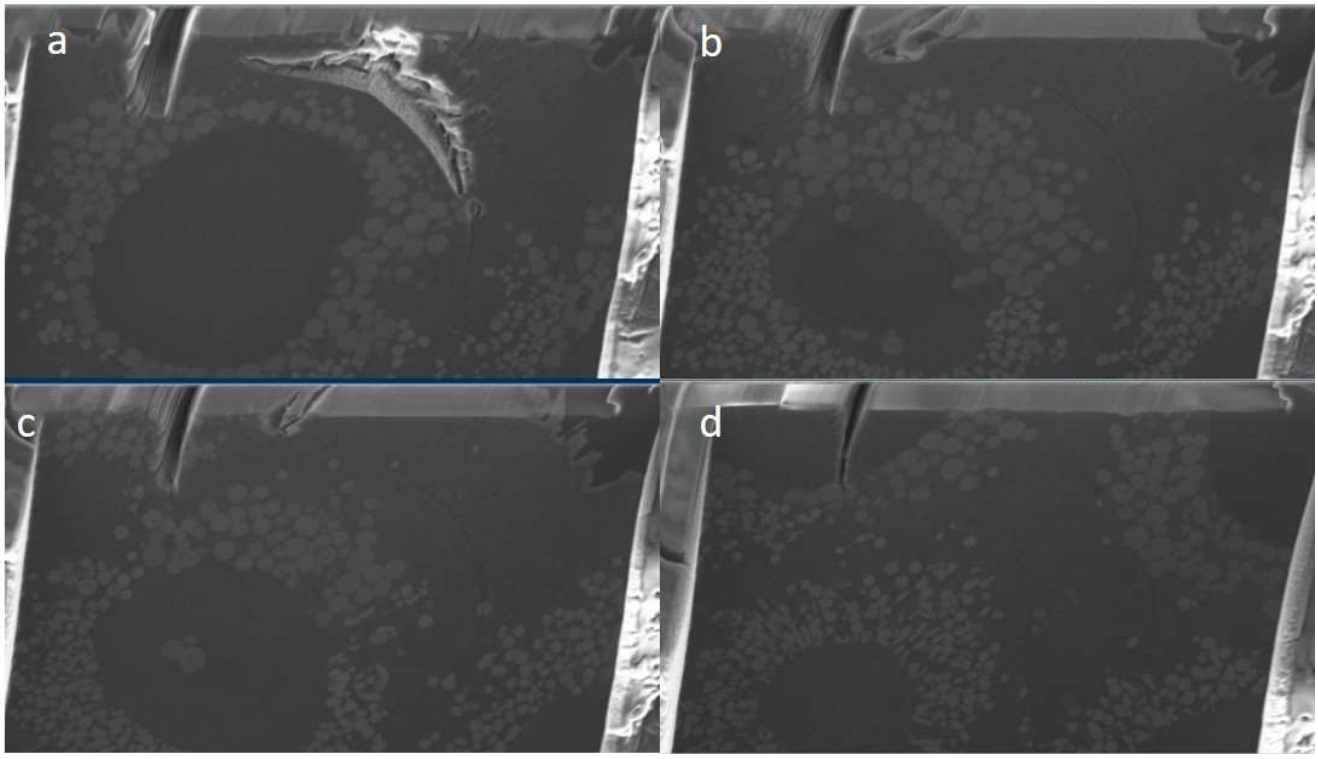

Figure 3.8: Different slice view of a single eyelet: (a): slice view from the top part of the eyelet; (b) and (c): slice view from the middle part of the eyelet; (d): slice view just before the eyelet finished

data treatment

Once we got the raw data, we were interested in having a 3D model out of it in order to get more visual information. We did this using ImageJ software. By using the threshold option, we got rid away of most of the non-pigment related pixels. The best fitting method has been Shanbhag [31]. We placed the cutoff on the intensity of the pixel at 110. It is the value which cut more of the unwanted data such as etching artifact data point without cutting too much of the pigment-related data. We then use the analyze particle module to get rid away of even more of the non-pigment group of pixels (particles). Our selection was

there made on the circularity of the particle. The circularity is defined by the formula 3.1 ([32]).

$$circularity = 4 * \pi * \frac{area}{perimeter^2} \tag{3.1}$$

By applying the formula for a perfect circle perimeter and area, we see that it will return one for such a shape. The more the shape of the particle differs from a circle, the closest to zero this parameter will be. We exclude all the particle with a circularity parameter smaller than 0.1. Our first threshold attempt was not perfect and some detectors have been group into the same particle. In order not to exclude them from the final picture we choose this value which is still high enough to exclude the etching lines but low enough to not removing too many pigments.

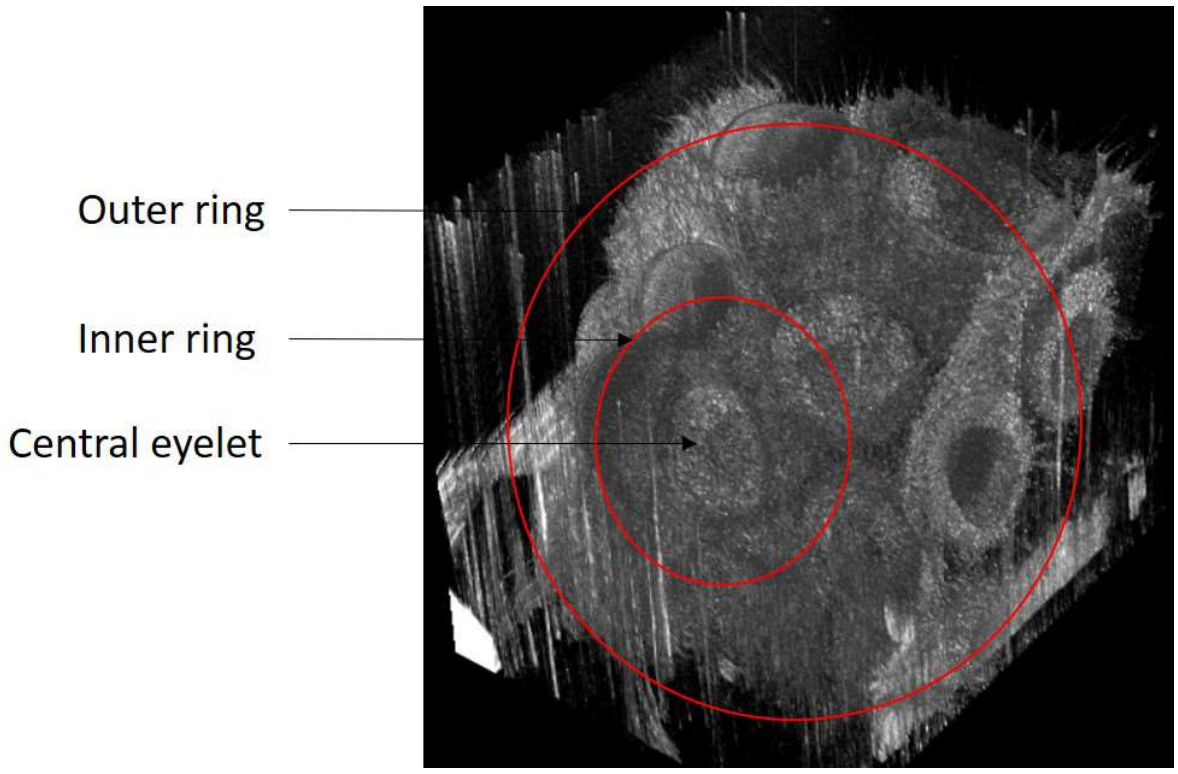

Figure 3.9: 3D view of a full eye after treatment

Figure 3.9 show the remaining image after we went through the whole procedure on the first set of data we acquired. We can see on figure 3.9 that, as explained before, the eye is composed of several eyelets

and they are located on three different circles. Because the etching area was too small, we missed some of the eyelets. This is why there are not seven eyelets on the inner circle and not eleven of them on the outer ring. Once we processed the whole eye data set, we applied the same treatment on the second data set, the one where we focused on a single eyelet with a smaller z step. Here we are looking for the retina of the eyelet. However, it is not visible in the raw data because the contrast is too low due to the preparation of the sample. As it was originally meant to be observed under the Transmission Electron Microscope and not the SEM, the specimen has been more lightly stained and therefore the contrast cannot be as high as it should be in order to see directly the retina. The staining process is to include some metal in the specimen to increase the contrast. Indeed, as both the specimen and the resin are carbon-based material, we have a low composition contrast. The goal here is to create a mask of the pigment in the eyelet and to subtract it from the original data set. The retina should be in the remaining information. Unfortunately, as one can see on figure 3.10, we could not find an optimal setup for the thresholding and therefore a lot of the data is missing. This is the reason why so many layers are missing at the bottom of the 3D model. We tried different parameters both for the pixel threshold and for the particle analyzes conditions but could not get a suitable image of the retina.

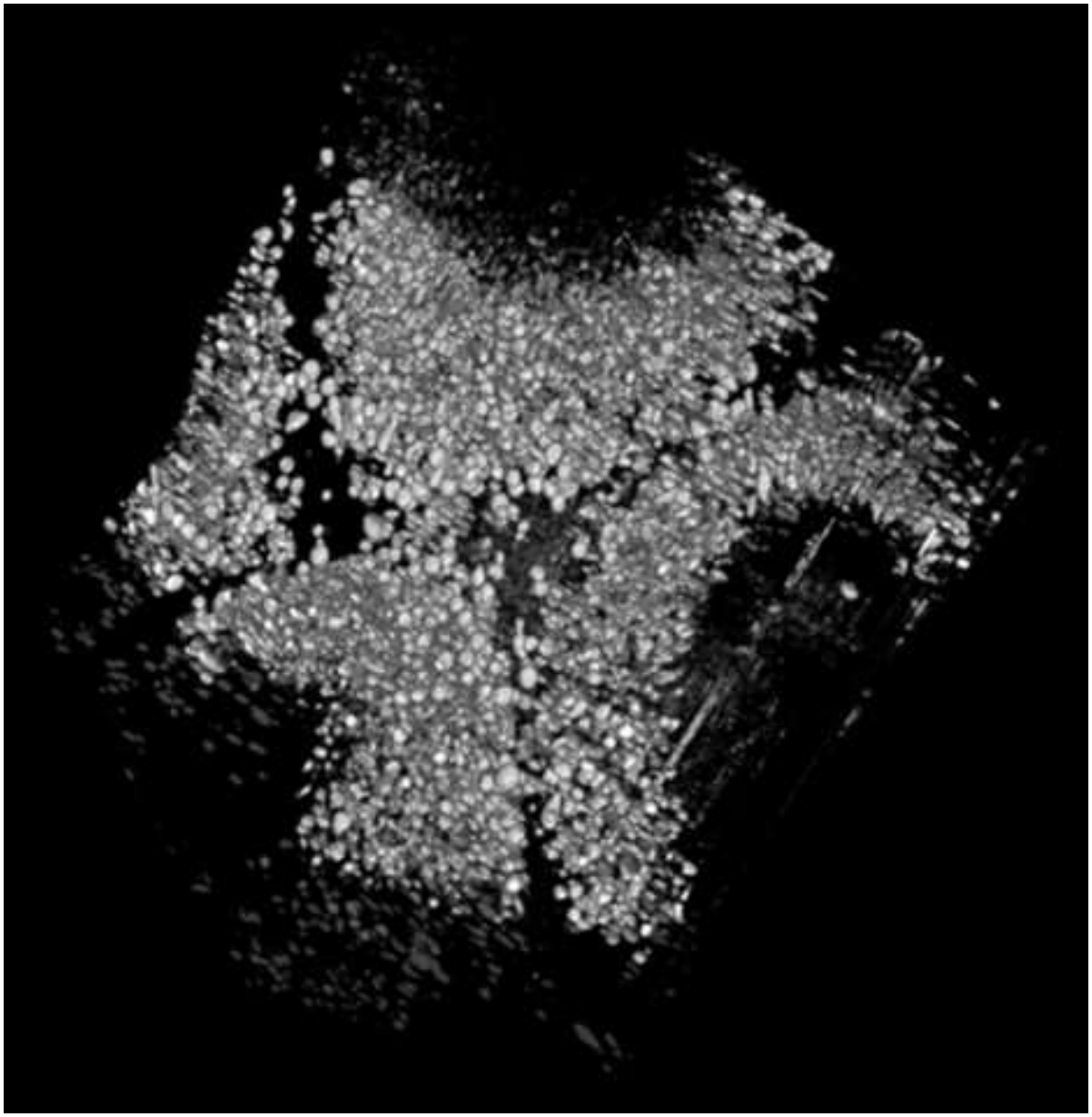

Figure 3.10: 3D view of high resolution data set of inner ring eyelet after treatment

3.4 Conclusion

In this chapter, different Strepsiptera eye structures have been imaged using the FIB-SEM Zeiss Neon. Two data sets have been obtained. The information they contain as well as the knowledge acquired on the way to treat them by ImageJ could be helpful for further work. Even though, we did not collect enough information to determine the eye category, we learned that the distribution of pigment in the eyelet is function of the depth. On the outside of eyelet, the pigments are large and circular but as we get closer to the retina, it becomes stretched, smaller and reflective.

Bibliography

[1] G. T. P. Frigeri, L. Seravalli and S. Franchi, "Molecular beam epitaxy: An overview," *Comprehensive Semiconductor Science and Technology*, vol. 3, no. 12, pp. 480–522, 2011.

[2] C. Correge, "State of the art scanning electron microscope for multiple application: From solarcelles to megaspore," Master's thesis, University of Oklahoma, 2016.

[3] V. K. Peddinti, "Light emitted diodes (leds)," 2008.

[4] S. A. O. Kwong Yam, Li Li Low and Z. Hassan, "Gallium nitride: An overview of structural defects," *Optoelectronic - Materials and technique*, pp. 99–136, 2011.

[5] S. E. Ruzin, *Plant Microtechnique and Microscopy*. Oxford University Press, 1999.

[6] B. J. Griffin, "A comparison of conventional everhart-thornley style and in-lens secondary electron detectors - a further variable in scanning," *The journal of scanning microscopies*, vol. 33, pp. 162–173, 2011.

[7] J. G. et al, *Scanning Electron Microscopy and X-Ray analysis, Third editon*. Kluwer Academic 1 Plenum Publishers, 2003.

[8] D. E. N. David C. Joy and D. L. Davidson, "Electron channeling patterns in the scanning electron microscope," *Journal of Applied Physics*, vol. 53, no. 8, 1982.

[9] T. Maitland, "Electron backscattered diffraction," *Advanced Materials & Processes*, 2004.

[10] Y. G. A. V.-C. D. W. L. H. A. W. A. W. T.B. Britton, J. Jiang, "Tutorial: Crystal orientations and ebsd or which way is up?," *Materials Characterization*, vol. 117, pp. 113–126, 2016.

[11] R. N. Jagtap and A. H. Ambre, "Overview literature on atomic force microscopy (afm): Basic and its important applications for polymer characterization," *Indian Journal of Engineering and Materials Science*, vol. 13, pp. 368–384, 2006.

[12] K. S. WICKRAMASINGHE, *MOLECULAR BEAM EPITAXY OF ANTIMONY QUANTUM WELLS FOR PROBING TOPOLOGICAL SURFACE STATES*. PhD thesis, UNIVERSITY OF OKLAHOMA, 2017.

[13] E. O. GOBEL and K. PLOOG, "Fabrication and optical properties of semiconductor quantum wells and superlattices," *Progress in Quantum Electronics*, vol. 14, pp. 289–356, 1989.

[14] M. Fruchart and D. Carpentier, "An introduction to topological insulators," *Comptes Rendus Physique*, 2013.

[15] H. M. Dietrich Widmann and H. Friedrich, *Technology of Integrated Circuits*. Springer-Verlag, 2000.

[16] Zeiss website Can be found at: https://www.zeiss.com/microscopy/int/products/fib-sem-instruments/crossbeam/crossbeam-technology.html.

[17] K. N. . S. Subramaniam, "Focused ion beams in biology," *NATURE*, 2015.

[18] F. W. Y. Z. Zhicheng Xu, Jianxin Chen and L. He, "High-performance inas/gaassb superlattice long wavelength infrared photodetectors grown on inas substrates," *Semiconductor Science and Technology*, vol. 32, no. 5, 2017.

[19] I. Vurgaftman and J. R. Meyer, "Band parameters for iiiv compound semiconductors and their alloys," *Journal of Applied Physic*, vol. 89, no. 5815, 2001.

[20] R. People and J. C. Bean, "Calculation of critical layer thickness versus lattice mismatch for gexsi(1-x)/si strained-layer heterostructures," *Applied Physic Letters*, 1985.

[21] D. P. Larson, "Sem class," 2017.

[22] G. E. Lloyd, "Atomic number and crystallographic contrast images with the sem: a review of backscattered electron techniques," *Mineralogical Magazine*, vol. 51, no. 359, 1987.

[23] J. M. W. D. M. Albrecht, S. Christiansen and H. P. Strunk, "Surface ripples, crosshatch pattern, and dislocation formation: Cooperating mechanisms in lattice mismatch relaxation," *Applied Physic Letters*, vol. 67, pp. 289–356, 1995.

[24] Carl Zeiss NTS GmbH, *Software Manual SmartSEM V05.05*, 2011.

[25] R. Fuierer, *Procedural Operation Manualette*. Asylum Research, 2009.

[26] M. Fox and R. Ispasoiu, *Quantum Wells, Superlattices, and Band-Gap Engineering*. Springer, Cham, 2017.

[27] W. D. F. L. PengFei Zhang, Zheng Liu and J. Wu, "Topological and electronic transitions in a sb(111) nanolm: The interplay between quantum connement and surface effect," *Physical review B*, 2012.

[28] B. E. Elke Buschbeck and R. Hoy, "Chunk versus point sampling: Visual imaging in a small insect," *Science Mag*, 1999.

[29] B. E. E. K. Buschbeck and R. R. Hoy, "The unusual visual system of the strepsiptera: external eye and neuropils," *Journal of Comparative Physiology*, 2003.

[30] C.A.Volkert and A. Minor, "Focused ion beam microscopy and micromachining." MRS Bulletin, May 2007.

[31] A. G. Shanbhag, “Utilization of information measure as a means of image thresholding,” *Graphical models and image processing*, vol. 56, no. 5, pp. 414–419, 1994.

[32] T. Ferreira and W. Rasband, *ImageJ User guide*, 2012.